# Inhomogeneous and homogeneous broadening of excitonic spectra due to disorder

Philipps Universität Marburg

Dissertation
zur Erlangung des Doktorgrades
der Naturwissenschaften
(Dr. rer. nat.)

dem Fachbereich Physik
der Philipps-Universität Marburg
vorgelegt

von
**Noémi Gőgh**
aus Orosháza
(Ungarn)

Marburg/Lahn, 2009

Vom Fachbereich Physik der Philipps-Universität Marburg
als Dissertation angenommen am: 01.07.2009

| | |
|---|---|
| Erstgutachter: | Prof. Dr. Peter Thomas |
| Zweitgutachter: | Prof. Dr. Florian Gebhard |

Tag der mündlichen Prüfung: 09.07.2009

# Contents

# Introduction

Semiconductor heterostructures always show a certain degree of disorder. This disorder influences the optical properties of these materials. For not too strong disorder the spectra are dominated by the excitonic resonance. In an ordered structure this resonance is broadened only homogeneously. In the low-excitation limit it results from the electron-phonon coupling and from radiative decay. These processes are also called ”dephasing” and are characterized by a certain dephasing time $T_2$.

In a disordered material the excitonic line is in addition broadened inhomogeneously. This notion applies to independent optical resonances with different transition energies. It is less obvious, however, that disorder also contributes to homogeneous broadening.

It will be a major subject of this work, to study this ”disorder-induced dephasing”. Disorder induced dephasing has been predicted two decades ago [1, 2] for a semiconductor model where the many-particle Coulomb interaction has been ignored. In these studies it has been assumed, that disorder is so strong, that excitonic effects are less important if compared to disorder effects. For the opposite situation of weak disorder and dominant many-particle effects disorder-induced dephasing has been invoked in a theoretical study [3]. Different decays of Four-Wave-Mixing traces for parallel and cross linearly polarized excitation situations have been treated there. However, a clear illustration of this effect and explanation of its origin for semiconductors with weak disorder is missing so far.

When theoretically studying the optical properties of disordered semiconductor structures one meets the following major challenge: Not only the many-particle Coulomb interaction has to be implemented and dealt with in a consistent way, also the description of the disorder needs special attention. It is of utmost importance to treat both interactions on the same level, since it is their combined action which determines the linear and nonlinear optical spectra. Although analytical or numerical methods exist, which treat various aspects of the problem of excitonic spectra in disordered semiconductors [1–17] (for a review see, e.g., [18]), a satisfactory solution of this task has not been achieved so far. Also in this work, which concentrates on a numerical approach, we will experience severe limitations due to finite computer resources.

Two theoretical approaches have been used in the past to study optical properties of disordered semiconductors. One can calculate the configurational averaged optical polarization from its equation of motion. This is usually performed in a single-particle $k$-space basis or in a basis of excitonic relative-motion states. One obtains a set of equations that is not closed. Thus, approximations are necessary. The second approach is based on a tight-binding model which is formulated in real space [18]. The optical polarization is calculated for many realizations of disorder and at the end the configurationally averaged polarization is obtained by superposition. This approach is, besides model assumptions, free of approximations. It can thus be used to test the validity of the approximations necessary in the above mentioned approach. It should be noted, that the order in which the Coulomb interaction is included is dictated by the experiment if coherent optical experiments are considered (i.e., linear response $\chi^{(1)}$, Four-Wave-Mixing $\chi^{(3)}$). Thus, as far as coherent features are concerned, there is no problem with the Coulomb interaction in both approaches mentioned above.

My thesis is organized as follows. First, in Chapter 1, the linear optical absorption is studied as a function of various disorder parameters. For this study the Hartree-Fock limit for the many-particle interaction is exact. We will apply, to the same model, both an approach where the configurationally averaged optically polarization is calculated approximately, and a tight-binding approach with successive averaging, which is free of approximations. It will turn out, that the first approach needs two independent approximations in order to yield physically reasonable results for the linear spectrum. We find that, although the cross features of the linear spectra for both approaches agree quite reasonably, there are finer details, where we see conflicting results. As a consequence, we only use the tight-binding real-space model for the detailed study of disorder-induced features in the linear and nonlinear excitonic spectra for the rest of this work. Compared to the first method its disadvantage is the much larger numerical effort due to the subsequent configurational averaging. It will be illustrated that, in particular, the length scale of the disorder potential plays an important role. It determines both the width of the linear spectrum and its shift relative to the position of the ordered counterpart.

In Chapter 2 disorder-induced features in nonlinear excitonic spectra are studied. We have in mind the experimental technique "Two-Dimensional Fourier-Transform Spectroscopy" (2DFTS), which has recently been applied to semiconductors in the optical regime [15, 19–21]. This technique is a variant of Four-Wave-Mixing and, for low excitation conditions, can be treated in the coherent $\chi^{(3)}$-limit. In contrast to experiments in the linear regime nonlinear experiments provide the possibility to determine both inhomogeneous and homogeneous broadening independently [18]. In addition, from the spectral features in the resulting two-dimensional plots one can identify various couplings between optical transitions, such as due to common ground state, Hamiltonian coupling like coherent tunneling, many-particle induced exciton-biexciton coupling, etc. Since in a disordered environment the $k$-selection rule is violated, there appear disorder-induced couplings that are absent in the ordered counterpart. It is these couplings that lead to interesting mechanism like "disorder-induced dephasing" and energy dependent dephasing within an inhomogeneous line. These mechanisms will be studied and interpreted in detail. To this end we introduce the scenario of Fano-coupling in the frame of 2DFTS. On the basis of a simple level system the features in 2DFTS that can be expected from Fano-coupling are illustrated.

The thesis ends with a conclusion and an outlook. Extensive equations that have been used during this study are collected in the Appendix in order to make the main text more easily readable.

# 1 Linear absorption

In this work optical properties of disordered semiconductors are studied theoretically. In particular, excitation of a direct semiconductor heterostructure by a classical light field is considered. Here transitions in the energy range around the fundamental gap are treated. In the case of optical excitation, the energies of the photons have to be sufficient to excite electron-hole pairs. These pairs can form bound pairs, called excitons, or for larger excitation energy, Coulomb-correlated pairs. Such an excitation not only generates an electron-hole pair but is also accompanied by the creation of the microscopic optical polarization. The sum of all microscopic polarizations provides the macroscopic polarization of the material. This macroscopic polarization is proportional to the light field in the regime of linear response and defines the linear optical susceptibility $\chi(\omega)$ by

$$P(\omega) = \chi(\omega)E(\omega). \tag{1}$$

The optical susceptibility is a complex quantity

$$\chi(\omega) = \chi'(\omega) + i\chi''(\omega) \tag{2}$$

and obeys the Kramers-Konig relations. On the other hand, we know that the absorption coefficient can be calculated from the optical susceptibility by

$$\alpha(\omega) = \frac{4\pi\omega}{n(\omega)c}\chi''(\omega) \approx \frac{4\pi\omega}{n_b c}\chi''(\omega) \approx \frac{4\pi\omega_0}{n_b c}\chi''(\omega), \tag{3}$$

where $c$ is the velocity of the light in vacuum, and we assumed that the refractive index $n(\omega)$ is just a constant background value $n_b$ in the limited photon energy interval around $\omega_0$ considered. Thus, up to a constant prefactor, the absorption is given by the imaginary part of the macroscopical polarization as

$$\alpha(\omega) \propto \chi''(\omega) = \mathbf{Im}\left(\frac{P(\omega)}{E(\omega)}\right). \tag{4}$$

As stated above, the macroscopic polarization is the sum of the microscopic polarizations $p_{kk}$,

$$P = \sum_k d^*_{vc}(k)p_{kk} + h.c., \tag{5}$$

where $d_{vc}(k)$ is the optical interband dipole matrix element. Thus we need to calculate the microscopic polarization $p_{kk}$, where $k$ is the particle's crystal momentum.

## 1.1 Equation of motion method

For the theoretical analysis the equation of motion approach is applied. This is based on the Heisenberg equation,

$$i\hbar \frac{\partial O}{\partial t} = [O, H] = OH - HO, \tag{6}$$

which describes the time evolution of any operator $O$.

In quantum physics the polarization corresponds to the expectation value of the polarization operator. This can be written as

$$\langle p_{kl} \rangle = \langle v_k^\dagger c_l \rangle, \tag{7}$$

where $v_k^\dagger$ creates an electron in the valence band, and $c_l$ annihilates an electron in the conduction band. The electron-electron picture is used.

In this work the system Hamiltonian is composed of the following terms: the single-particle kinetic part, the Coulomb term describing many-particle interaction, the interaction with the light field, and the term describing scattering at the disorder. Any other interaction is not considered here.

## 1.2 $k$-space model

Semiconductor optics is generally treated in the framework of the momentum-($k$)-space model [22–24]. This is because for a perfect semiconductor there exists a quantum number $k$ which describes the electronic states due to translational symmetry. I.e., we have momentum conservation. Thus, a single index $k = k'$ is sufficient for the description of optical transitions due to the vanishing small momentum of the photon.

In theoretical work treating optical properties of disordered semiconductors on the basis of the k-space model, the configurationally averaged optical polarization is usually considered (see, e.g., [4, 5]), and $k = k'$ is also sufficient here.

The presentation in this work starts with the $k$-space description in the electron-electron picture. A two-band model is treated with a conduction band $c$ and a valence band $v$. In the ground state of a semiconductor all electrons occupy the fully filled valence band while the conduction band is empty. Although, the optical excitation lifts carriers from the valence to the conduction band, we apply the low density limit where only the optical polarization is important and excited densities can be neglected [18]. They are given in at least second order in the light field.

Throughout this work explicit spin effects are also neglected. The spin only enters the optical selection rule, when nonlinear spectra are considered in Chapter 2.

Furthermore, to keep the presentation of this fundamental study as simple as possible and due to numerical limitations, we confine ourselves to a one-dimensional model.

### 1.2.1 System Hamiltonian

The system Hamiltonian consists of four terms:

$$H = H_{kin} + H_C + H_L + H_{dis}. \tag{8}$$

**Kinetic part**
The kinetic part contains the single particle Hamiltonian

$$H_{kin} = \sum_k \left( \varepsilon_k^c c_k^\dagger c_k + \varepsilon_k^v v_k^\dagger v_k \right). \tag{9}$$

We assume a quadratic dispersion relation, thus the single-particle energies are given by

$$\varepsilon_k^c = \frac{\hbar^2 k^2}{2m^e} + E_G, \tag{10}$$

$$\varepsilon_k^v = -\frac{\hbar^2 k^2}{2m^h}, \tag{11}$$

where $m^e$ and $m^h$ are the (positive) effective electron and hole masses in the conduction and valence band, respectively. Furthermore, $E_G$ denotes the direct bandgap. For GaAs/AlGaAs quantum wells, e.g., we take $m^e/m^h = 0.15$.

**Light-matter interaction**
To treat the light field a semiclassical picture is used. I.e., the classical electric light field $E(t)$ creates electron-hole transitions. The material part is quantized:

$$H_L = -E(t) \sum_k (d_{vc}(k) v_k^\dagger c_k + d_{vc}(k)^* c_k^\dagger v_k). \tag{12}$$

We neglect the vectorial character of both the electric field and the dipole matrix elements, assuming implicitly an isotropic case and no spin dependent effects.

**Coulomb term**
In order to describe the many-particle Coulomb interaction between the optically

generated electrons and holes, we use the Hamiltonian

$$H_C = \frac{1}{2} \sum_{\substack{k_1,k_2,\\ q\neq 0}} V_q \left( c^\dagger_{k_1} c^\dagger_{k_2} c_{k_2+q} c_{k_1-q} + v^\dagger_{k_1} v^\dagger_{k_2} v_{k_2+q} v_{k_1-q} + 2 c^\dagger_{k_1} v^\dagger_{k_2} v_{k_2+q} c_{k_1-q} \right), \tag{13}$$

where $V_q$ is the Coulomb-matrix element (details see Appendix B). The first two terms correspond to the repulsive interaction between the electrons within the same band, while the last term leads to the attractive interaction between the electrons and holes in different bands.

**Disorder Hamiltonian**

$H_{dis}$ describes the interaction of the electronic system with the static disorder

$$H_{dis} = \sum_{k_1,k_2} \left( U^v_{k_1-k_2} v^\dagger_{k_1} v_{k_2} + U^c_{k_1-k_2} c^\dagger_{k_1} c_{k_2} \right). \tag{14}$$

This leads to the scattering of the electrons and holes at the disorder potential which is described by the disorder matrix elements ($U_k^{c/v}$).

For the correlation function of the disorder potential we base our calculations on the following Gaussian form, previously used by A. Thränhardt [4, 5] for the description of disordered two-dimensional quantum wells. In our one-dimensional model it reads:

$$\langle U_k^\lambda U_{k'}^{\lambda'} \rangle_E = \frac{\pi^4 \hbar^4 \gamma^2 \xi \sqrt{\pi}}{\mathcal{L} L_w^6 m^\lambda m^{\lambda'}} \delta_{k,-k'} e^{-\frac{k^2 \xi^2}{4}}, \tag{15}$$

where: $\gamma$: the magnitude of the fluctuation of the disorder amplitude
$\xi$: the disorder length scale
$\mathcal{L}$: the quantization length
$L_w$: the well width
$m^\lambda$: the effective mass in band $\lambda$.

Thus for the two band model it has the form

$$\langle U_k^\lambda U_{k'}^{\lambda'} \rangle_E = A \delta_{k,-k'} e^{-k^2 B}. \tag{16}$$

Here $\{\lambda, \lambda'\} = \{c, v\}$, $c$ denotes the conduction band, and $v$ denotes the valence band.

After the optical excitation, the coherent features, e.g., the polarization decays on a picosecond time scale. In order to include the dephasing effects due to the interaction with other, here not considered quasi-particles and scatterings, we introduce a phenomenological dephasing time ($T_2$). Throughout this study this dephasing time was chosen such that it causes 1.37 meV homogeneous broadening in the ordered case.

In the following presentation we use a simplified notation in the equations. Detailed derivations and forms can be found in the cited Appendices.

### 1.2.2 Hierarchy problem

**Coulomb hierarchy**

When we explicitly evaluate the commutator in the equation of motion for the polarization we find that it couples to new operators due to the Coulomb term. These have a more complicated structure than the original polarization operator. If the equation of motion for this new operator is derived, we find even higher-order operators, etc. One $N$-point operator quantity is coupled to an $N+2$ point operator. This leads to the well known hierarchy problem [18, 24–28]:

$$\begin{aligned} i\hbar\frac{\partial}{\partial t}\langle a^\dagger a\rangle &= \langle a^\dagger a\rangle + \langle a^\dagger a^\dagger aa\rangle && (17)\\ i\hbar\frac{\partial}{\partial t}\langle a^\dagger a^\dagger aa\rangle &= \langle a^\dagger a^\dagger aa\rangle + \langle a^\dagger a^\dagger a^\dagger aaa\rangle && (18)\\ &\vdots \end{aligned}$$

We arrive at an infinite set of equations, which cannot be solved. We need to truncate it somehow. One successful approach is the so-called cluster expansion method [24], Appendix C. In this Chapter we stop at the Hartree-Fock (HF) level, because for absorption the Hartree-Fock approximation is exact, as we are in the linear response regime (see, e.g [18]).

$$\begin{aligned} \langle a_1^\dagger a_2^\dagger a_3 a_4\rangle &= \langle a_1^\dagger a_4\rangle\langle a_2^\dagger a_3\rangle - \langle a_1^\dagger a_3\rangle\langle a_2^\dagger a_4\rangle + \Delta\langle a_1^\dagger a_2^\dagger a_3 a_4\rangle && (19)\\ \langle a_1^\dagger a_2^\dagger a_3 a_4\rangle\Big|_{HF} &= \langle a_1^\dagger a_4\rangle\langle a_2^\dagger a_3\rangle - \langle a_1^\dagger a_3\rangle\langle a_2^\dagger a_4\rangle. && (20) \end{aligned}$$

**Disorder hierarchy**

Using our Hamiltonian we find that the disorder term generates another hierarchy problem. The structure of this set of equations is

$$\begin{aligned} i\hbar\frac{\partial}{\partial t}\langle P\rangle_E &= \ldots\langle P\rangle_E + \ldots\langle UP\rangle_E + \ldots && (21)\\ i\hbar\frac{\partial}{\partial t}\langle UP\rangle_E &= \ldots\langle UP\rangle_E + \ldots\langle UUP\rangle_E && (22)\\ i\hbar\frac{\partial}{\partial t}\langle UUP\rangle_E &= \ldots\langle UUP\rangle_E + \ldots\langle UUUP\rangle_E && (23)\\ &\vdots \end{aligned}$$

Here $\langle\cdot\rangle_E$ denotes the ensemble average. The polarization $\langle P\rangle_E$ couples to the disorder assisted polarization $\langle UP\rangle_E$, etc. Thus we need to derive the equations of motion for these new quantities as well. We again obtain an infinite set of equations. Since the cluster expansion was successful in the Coulomb-induced hierarchy problem, we try to use a similar approach here, which is called second-Born approximation. The disorder-assisted quantities are factorized in the following way [4,5]:

$$\begin{aligned}\langle U_1 U_2 P\rangle_E =& \langle U_1\rangle_E \langle U_2 P\rangle_E + \langle U_2\rangle_E \langle U_1 P\rangle_E \\ &+ \langle U_1 U_2\rangle_E \langle P\rangle_E + \Delta\langle U_1 U_2 P\rangle_E.\end{aligned} \tag{24}$$

### 1.2.3 Second-Born approximation

Applying the second-Born approximation we leave out the correlation part $\Delta\langle U_1 U_2 P\rangle_E$ from the factorization above:

$$\begin{aligned}\langle U_1 U_2 P\rangle_E =& \langle U_1\rangle_E \langle U_2 P\rangle_E + \langle U_2\rangle_E \langle U_1 P\rangle_E \\ &+ \langle U_1 U_2\rangle_E \langle P\rangle_E.\end{aligned} \tag{25}$$

The first two terms vanish because the ensemble averages of the disorder matrix elements are taken to be zero. Thus we write approximately

$$\langle U_1 U_2 P\rangle_E = \langle U_1 U_2\rangle_E \langle P\rangle_E. \tag{26}$$

We than arrive at a closed set of equations of the form

$$i\hbar\frac{\partial}{\partial t}\langle P\rangle_E = \ldots\langle P\rangle_E + \ldots\langle UP\rangle_E + \ldots \tag{27}$$

$$i\hbar\frac{\partial}{\partial t}\langle UP\rangle_E = \ldots\langle UP\rangle_E + \ldots\langle UU\rangle_E\langle P\rangle_E. \tag{28}$$

Solving this set of equations yields a double peaked spectrum for every excitonic resonance, see Fig. 1(a), [29]. The lower energy peak is situated below the excitonic resonance of the ordered system, while the upper one is just above this resonance. This result is clearly unphysical. Its occurrence can be explained mathematically (See in Appendix F).

### 1.2.4 Markov approximation

Instead of solving the equation of motion for the disorder-assisted polarization, following Thränhardt [4,5] we now introduce the Markov approximation in addition (Appendix D). The double-peak structure now disappears.

In this combined second-Born - Markov approximation scheme the equation for the disorder-assisted polarization is formally integrated, $\langle p(t)\rangle_E$ is taken out of the integral, resulting in an effective damping. The equations read in more detail (see

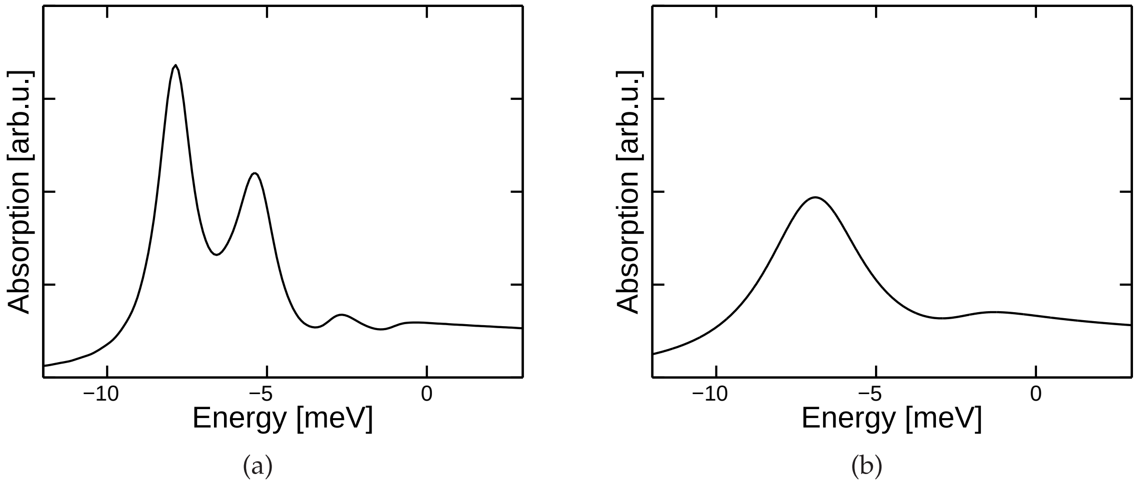

(a)

(b)

Figure 1: Calculated spectra with identical disorder, using (a) only the second-Born approximation, (b) second-Born and Markov approximation

Appendix E)

$$
\begin{aligned}
i\hbar\frac{\partial}{\partial t}\langle p(t)\rangle_E &= (\varepsilon_1 - i\gamma)\langle p(t)\rangle_E + \langle Up(t)\rangle_E - E(t)d^*_{vc} && (29)\\
i\hbar\frac{\partial}{\partial t}\langle Up(t)\rangle_E &= (\varepsilon_2 - i\gamma)\langle Up(t)\rangle_E + \langle UU\rangle_E\langle p(t)\rangle_E. && (30)
\end{aligned}
$$

From Eq. (30) we than obtain

$$
\langle Up(t)\rangle_E = \frac{\langle UU\rangle_E\langle p(t)\rangle_E}{\varepsilon_1 - \varepsilon_2 + i\gamma}. \tag{31}
$$

The solution of Eq. (29) with this result for the disorder-assisted polarization provides a spectrum, which we would expect for a disorder-broadened excitonic line (Fig. 1(b)). The Markov approximation generates a self-energy that has a much simpler structure than that following from just the second-Born approach (see Appendix F). Its imaginary part is nonzero everywhere, yielding a single-peaked spectrum.

### 1.2.5 Exciton basis

Instead of considering single-particle momentum ($k$)-states as a basis of our Hilbert space, we can alternatively use a basis formed from excitonic relative-motion two-particle states $\phi_\nu(\tilde{k})$. Here $\nu$ denotes the quantum number of the pair states and

$$
\tilde{k} = \frac{m^e}{M}k + \frac{m^h}{M}k' \tag{32}
$$

is the relative-motion momentum [25]. Here $k$ and $k'$ are the electron and hole momenta, respectively, and $M = m^e + m^h$.

This representation has several advantages. i) We are able to directly compare our results with those obtained in previous work [4, 6]. ii) This basis enables us to switch on and off the pair-continuum states. iii) We can even confine our study to just the lowest excitonic resonance, which in a three-dimensional system would be denoted by the "1s"-exciton. This allows us to discuss various spectral features most clearly.

We introduce the exciton creation and annihilation operators as follows:

$$\begin{aligned} X^\dagger_{\nu,q} &= \sum_{\tilde{k}} \phi_\nu(\tilde{k}) c^\dagger_{\tilde{k}+q^e} v_{\tilde{k}-q^h} && (33) \\ X_{\nu,q} &= \sum_{\tilde{k}} \phi^*_\nu(\tilde{k}) v^\dagger_{\tilde{k}-q^h} c_{\tilde{k}+q^e}, && (34) \end{aligned}$$

where $q^{e/h} = \frac{m^{e/h}}{M} q$, with the center-of-mass momentum $q = k' - k$, with $k$, $k'$ from Eq. (32). The relative-motion wave function $\phi_\nu(\tilde{k})$ is the solution of the homogeneous part of the Semiconductor-Bloch-Equations in the low-density limit (the Wannier equation) [30]:

$$\left(\frac{\hbar^2 k^2}{2\mu}\right) \phi_\nu(k) - \sum_{k'} V_{k'-k} \phi_\nu(k') = \varepsilon_\nu \phi_\nu(k), \tag{35}$$

where $\mu$ is the reduced mass ($\mu = \frac{m^e m^h}{m^e + m^h}$). The following orthogonality relation is valid:

$$\sum_k \phi^*_\nu(k) \phi_{\nu'}(k) = \delta_{\nu,\nu'}. \tag{36}$$

The configurationally averaged center of mass function of the excitonic resonance $\nu$ with momentum $q$ is denoted by $\langle X_{\nu q}(t) \rangle_E$ and gives the optical polarization. Here again the second-Born and Markov approximations will be applied (Appendix E).

## 1.3 Real-space tight-binding model

We continue the description with a real-space model. Here a one dimensional tight-binding model is used. The advantage of the real-space tight-binding model is, that it is numerically exact in principle, no further approximations are necessary [18].

Throughout this study the number of sites is chosen to be $N = 100$ and the site separation $a = 5$nm. That means, the size of the sample is 500nm. Periodic boundary conditions are used. The intraband couplings are denominated as $J^c$ and

$J^v$. $W^c$ and $W^v$ are parameters of the disorder of the conduction and valence bands, respectively. For an extensive discussion and justification of this model see [18].

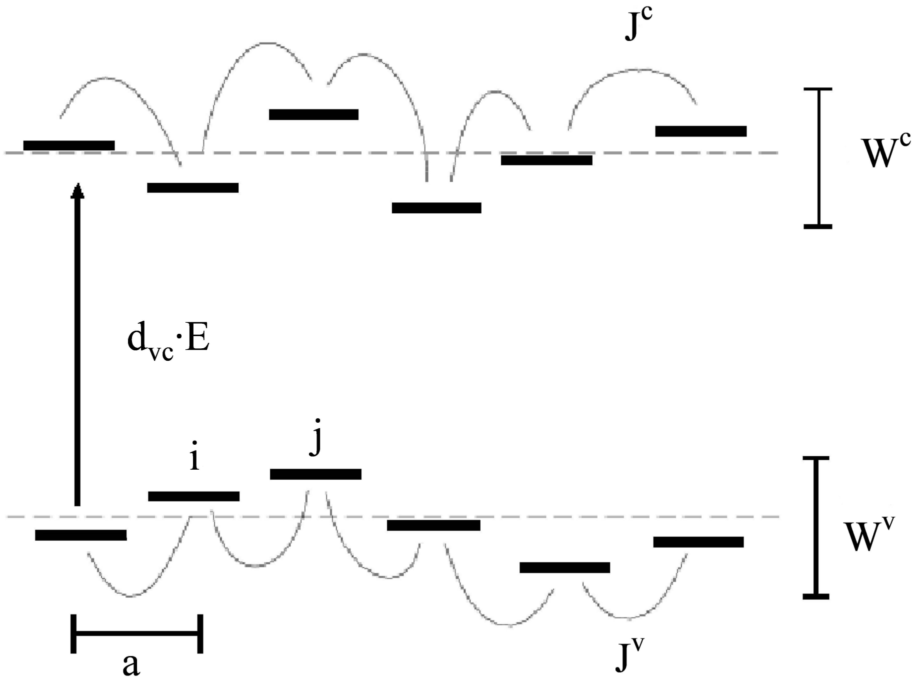

Figure 2: Tight-binding model

### 1.3.1 System Hamiltonian

The Hamiltonian in real-space representation consists of the same terms as that in the $k$-space model:

$$H = H_{kin} + H_L + H_C + H_{dis}. \tag{37}$$

The light-matter interaction and the Coulomb term have their conventional form:

**Light-matter interaction**

The light-matter interaction is treated again semiclassically

$$H_L = -E(t) \sum_j (d_{vc} v_j^\dagger c_j + d_{vc}^* c_j^\dagger v_j). \tag{38}$$

**Coulomb term**

The first two terms are the repulsive interactions, and the third one is the attractive interaction between the electrons and holes

$$H_C = \frac{1}{2} \sum_{i,j} V_{ij} \left( c_i^\dagger c_j^\dagger c_j c_i + v_i^\dagger v_j^\dagger v_j v_i + 2 c_i^\dagger v_j^\dagger v_i c_j \right). \tag{39}$$

The kinetic term and the disorder part of the Hamiltonian is treated as follows.

**Kinetic part**

$$H_{kin} = J^c \sum_j \left( c_j^\dagger c_{j-1} + c_j^\dagger c_{j+1} \right) + J^v \sum_j \left( v_j^\dagger v_{j-1} + v_j^\dagger v_{j+1} \right) \tag{40}$$

These terms describe the coupling between the nearest neighbor sites in the same band. $J^c$ and $J^v$ are the coupling constants in the conduction and valence band, respectively. They are related to the effective masses at the band extrema by

$$m^\lambda = \frac{\hbar^2}{2|J^\lambda|a^2}. \tag{41}$$

**Disorder**

The last part of the Hamiltonian describes the scattering at the disorder potential

$$H_{dis} = \sum_j \left( \varepsilon_j^c c_j^\dagger c_j + \varepsilon_j^v v_j^\dagger v_j \right). \tag{42}$$

We introduce disorder in the following way [7,31]: first we choose the energies randomly between two parameters ± W/2 around zero, where W is the width of the box-like distribution. This defines one realization. In the next step, after a Fourier-transform, a Gaussian filter is applied, and the result is transformed back into real-space. By this way a length scale of the disorder potential can be introduced. Fig. 4 shows disorder potentials with different length scale that originate from the same random potential. This method decreases the amplitude of the disorder, see Fig.5, thus we need to renormalize it, such that it has the same variance as the original potential. The equation of motion for the linear polarization is solved for any given realization of the disorder potential. The configurationally averaged optical polarization then follows from a superposition of the results for a large number (typically $M = 100$) of realizations.

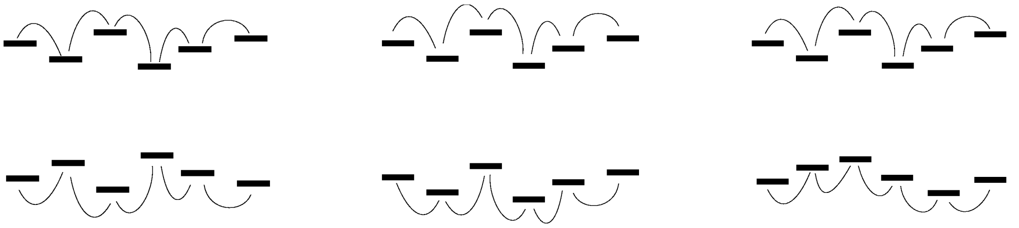
(a) correlated disorder (b) anticorrelated disorder (c) uncorrelated disorder

Figure 3: Different types of disorder

The disadvantage of this method lies in the fact that extensive averaging over

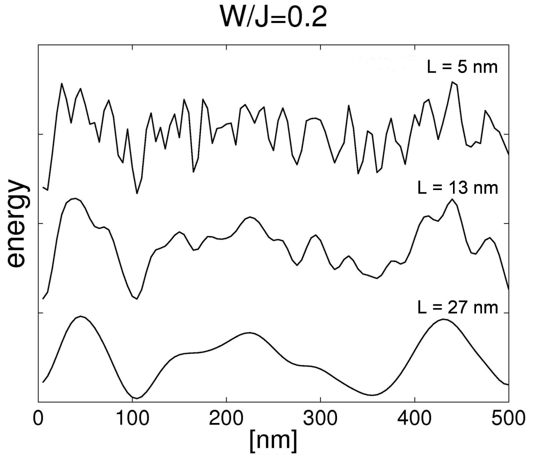

Figure 4: Representation of disorder potentials for different length scale $L$

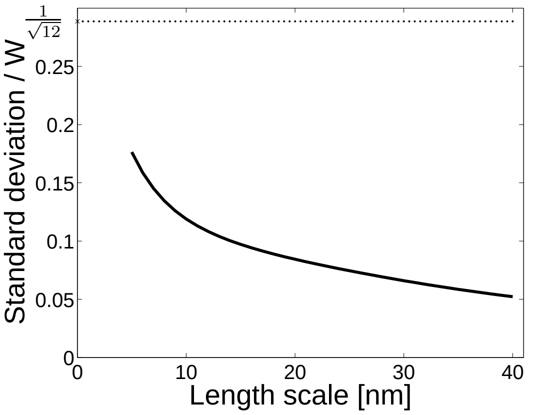

Figure 5: Standard deviation of the conduction-band disorder distributions for one realization without renormalization. For the original box distribution it is $W/\sqrt{12}$ (dotted line)

realizations of the disorder potential is necessary in order to achieve smooth spectra. This constitutes a numerical limitation to the calculations.

### 1.3.2 Equation of motion in real space

Using the Heisenberg equation, as before, we obtain the equation of motion of the linear polarization:

$$\begin{aligned} i\hbar\frac{\partial}{\partial t}p_{ij} =& (\varepsilon_j^c - \varepsilon_i^v)p_{ij} - V_{ij}p_{ij} - E(t)d_{vc}^*\delta_{ij} \\ & + J^c(p_{i,j-1} + p_{i,j+1}) + J^v(p_{i+1,j} + p_{i-i,j}) \end{aligned} \tag{43}$$

Introducing two matrices $T_{ij}^\lambda$ as follows:

$$\begin{aligned} T_{ii}^c &= \varepsilon_i^c && \text{and} \qquad T_{ii}^v = -\varepsilon_i^v \\ T_{ij}^{c/v} &= J_{ij}^{c/v} && \text{for nearest neighbors} \\ T_{ij}^{c/v} &= 0 && \text{else,} \end{aligned} \tag{44}$$

the equation of motion can be written as

$$i\hbar\frac{\partial}{\partial t}p_{ij} = \sum_l T_{jl}^c p_{il} + \sum_l T_{li}^v p_{lj} - V_{ij}p_{ij} - E(t)d_{vc}^*\delta_{ij}. \tag{45}$$

### 1.3.3 Elliott-formula

To speed up the numerical calculation, the equation of motion of the polarization is solved using the Elliott formula. Starting from the real-space Hamiltonian, the Wannier-equation is solved yielding the relative-motion wavefunctions $\phi_\lambda$ and eigenvalues $\epsilon_\lambda$. In this basis the equation of motion can be solved analytically, yielding [31]:

$$\chi''(\omega) = \sum_\lambda \frac{|\mu_\lambda|^2}{\epsilon_{bg}} \frac{\gamma}{(\varepsilon_\lambda - \hbar\omega)^2 + \gamma^2}, \tag{46}$$

where $\epsilon_{bg}$ is the dielectric background constant, $\mu_\lambda$ is the optical matrix element in two-particle basis, $\varepsilon_\lambda$ are the two-particle eigenenergies.

Alternatively, we also solved the equation of motion in the time domain in the single-particle basis. The results agreed, but it turned out, that this procedure is numerically more demanding.

## 1.4 Adjusting the $k$-space model to the real-space model

### 1.4.1 Correlation function

In order to treat the same model of disorder in both approaches we calculate the correlation function of the site-energy distribution function and transform it into $k$-space, yielding $F(k)$.

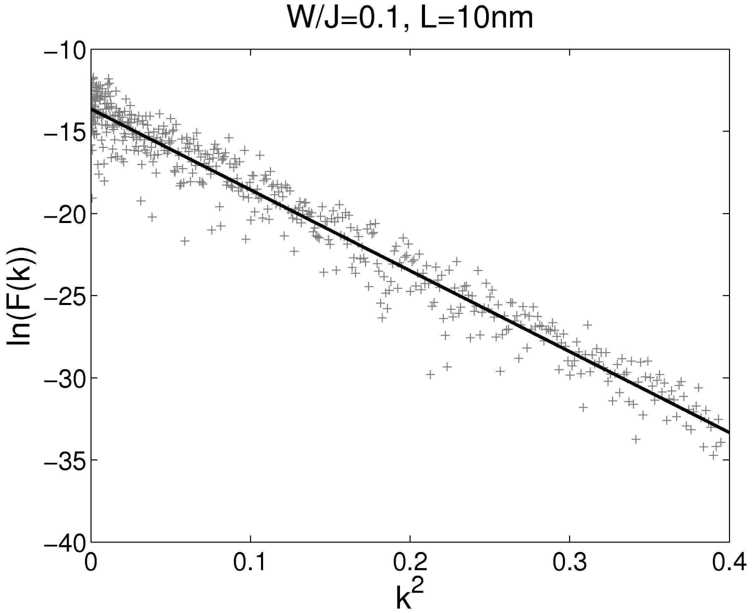

Figure 6: Logarithm of correlation function of site energies for $W/J = 0.1$ and $L = 10$ nm as a function of $k^2$

For a given realization $r$ of disorder the correlation function $F_{j,r}$ is defined as

$$F_{j,r} = \frac{1}{N} \sum_i \langle \varepsilon_{i,r} \varepsilon_{i+j,r} \rangle. \tag{47}$$

The site-energies $\varepsilon_{i,r}$ are the energies of site $i$ of the realization $r$. From these we can determine the averaged correlation function for $M$ realizations

$$F_j = \frac{1}{M} \sum_r F_{j,r}. \tag{48}$$

After a Fourier transformation we obtain $F(k) = \mathcal{FT}(F_j)$. When this is logarithmically plotted against $k^2$, we obtain a straight line, indicating a Gaussian distribution. From this we can determine the parameters $A$ and $B$ of the disorder-correlation function in $k$-space

$$\langle U_k^\lambda U_{k'}^{\lambda'} \rangle_E = A \delta_{k,k'} e^{-k^2 B}. \tag{49}$$

These two parameters $A$ and $B$ characterize the disorder completely in this model. The coefficient A scales with inverse masses $1/m^\lambda$ and $1/m^{\lambda'}$, according to Eq. 15. The masses follow from Eq. (41).

### 1.4.2 Comparison

We choose correlated disorder and

$$\frac{W^c}{|J^c|} = \frac{W^v}{|J^v|} = \frac{W}{J}. \tag{50}$$

In the first line of Fig. 7 the ratio $W/J$ of the disorder width and the coupling is smaller than in the second row.

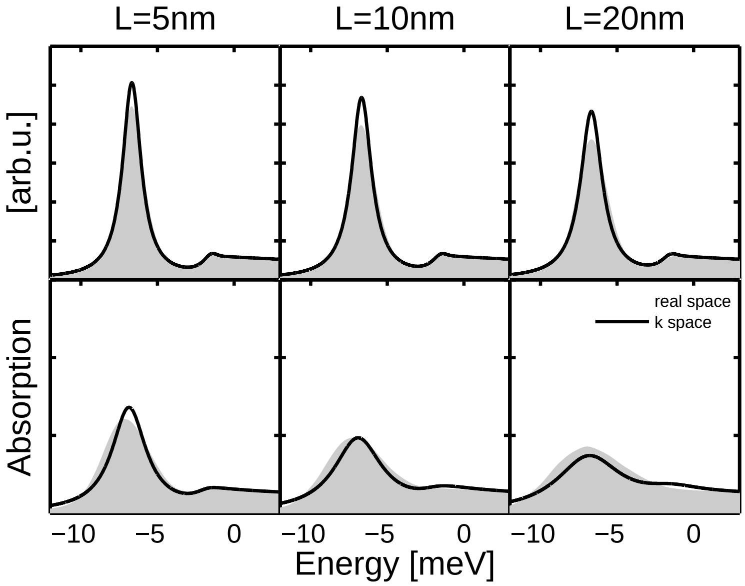

Figure 7: Linear spectra for different disorder amplitude and length scale. Gray: real-space model, solid line: k-space model. First row: $W/J = 0.1$, second row $W/J = 0.3$

As we can see, at first sight we have a qualitatively good agreement between the exact real-space model and the $k$-space calculation including the second-Born and Markov approximations. In the following, we will study finer features of the linear excitonic spectrum in order to judge the quality of the $k$-space model. To this end we start by a detailed discussion of shift and width (as a function of disorder parameters $W$ and $L$) obtained from the real-space model. Then some typical results for the $k$-space model are shown and critically compared to the real-space results.

## 1.5 Interplay of various length-scales

The features of the inhomogeneously broadened lines depend on the interplay of disorder and Coulomb effects. Both of them are characterized by a length scale. The disorder potential can be viewed as a static fluctuation of local potentials having a certain correlation length $L$. The Coulomb effects are characterized by the excitonic Bohr-radius $a_B$ [8].

Disorder does not only lead to a broadening of the lines, see Fig. 8. It also yields a shift of their maximum relative to that of the ordered case. This shift shows an characteristic dependence on length scale. This is exemplified in Fig. 9. In addition a typical asymmetric line shape is found in calculations of excitonic absorption lines for disordered systems [5, 6, 9, 10].

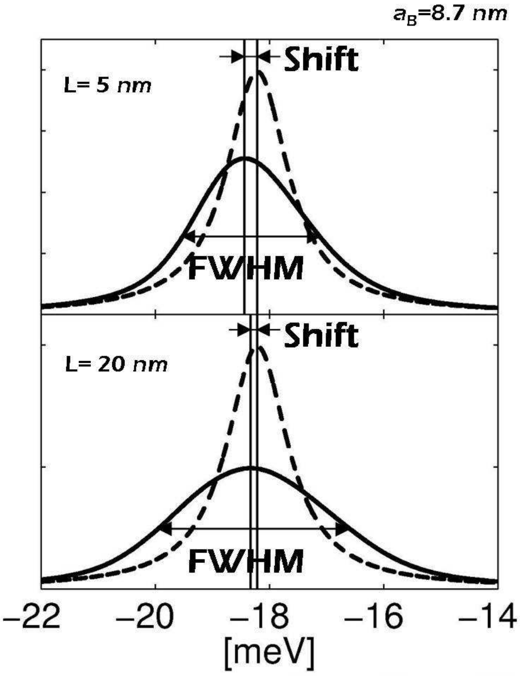

Figure 8: Illustrating broadening and shift of excitonic linear spectra due to disorder. Dashed lines indicate ordered case

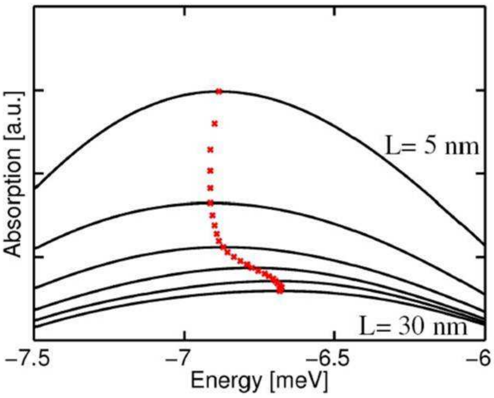

Figure 9: Magnified view of the shift of the maximum due to disorder. Here $a_B$=12,3nm, and various curves correspond to different $L$

Already in an ordered situation the excitonic line shape is not symmetric, but shows an exponential low-energy Urbach tail [11, 32–34] instead of the Lorentzian shape at higher energies. This is here due to the electron-phonon interaction and will not be treated in this work. Therefore, for the ordered situation we obtain a symmetric Lorentzian due to dephasing. It is assumed that sufficiently strong disorder effects by far dominate the line shape of the disordered situation. Thus we can neglect the Urbach tail here.

The line broadening depends on the nature of disorder. It is known [12] that alloy disorder has a different impact on the line shape compared to interface roughness. In this work we consider interface roughness as the dominant source of disorder in a semiconductor quantum structure.

### 1.5.1 Studied features - width and shift

In order to clearly identify the Coulomb-related features these quantities are plotted not only as a function of length scale $L$, but also against the ratio of length scale divided by the Bohr radius $L/a_B$.

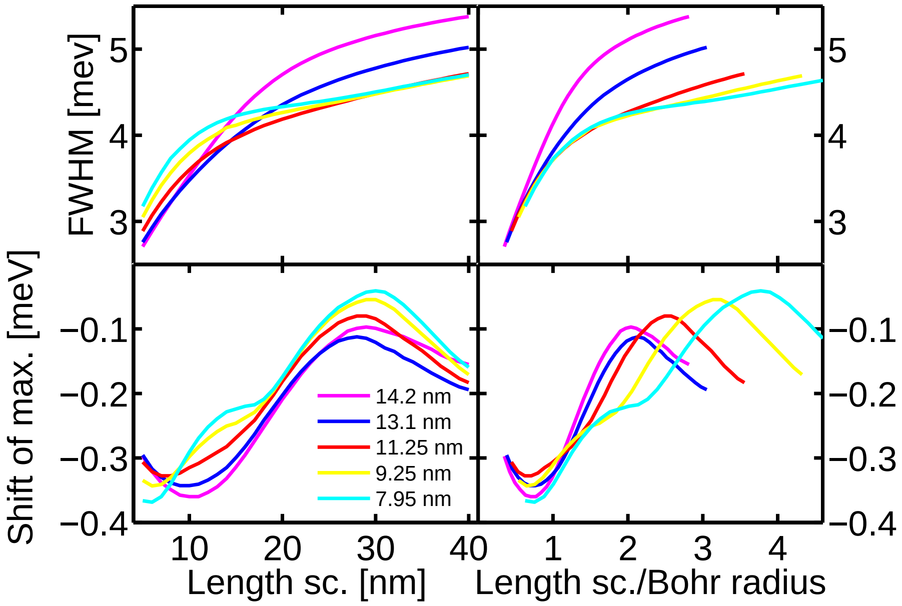

Figure 10: Upper row: width, lower row: shift, left hand column: plotted vs. $L$, right hand column: plotted vs. $L/a_B$. Various colors refer to Bohr radius $a_B$ as given in lower left figure

In the upper left figure of Fig. 10 we see that the width increases with disorder length scale monotonously. However, for different Coulomb strength, quantified by the Bohr radius as given in the lower left figure, there is no unique behavior. On the other hand, if we plot the width against $L/a_B$, a clear trend can be seen. For length scale less than the Bohr radius a seemingly universal behavior results, indicating that the spectra are indeed determined by the ratio of the length scale and the Bohr radius. For larger length scale a universal behavior is seen more clearly in the left hand figure, indicating, that here the role of the Coulomb effects is less dominant.

The lower part of the figure shows the shift of the maximum. Here it is important to realize, that the energy scale of this shift is much less than the full width at half maximum (FWHM). Obviously, the dependence of the shift on length scale is non-monotonous. Again we see different regimes. For length scale less than the Bohr radius the right hand figure indicates that there is a universal character, determined only by the ratio of length scale and Bohr radius. On the other hand, for increasing length scales beyond $a_B$, we have a blue shift followed by a red shift, and the Bohr radius does no longer influence the shift directly.

### 1.5.2 Influence of continuum

Since both, the FWHM and the shift are influenced by tails extending from the electron-hole pair continuum towards lower energies, in particular for small Coulomb strength (large Bohr radius and small binding energy), the excitonic spectra are influenced by these continuum transitions in the tail region.

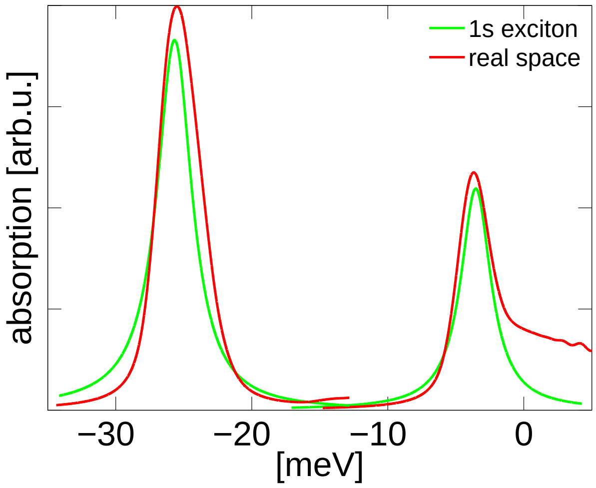

Figure 11: Excitonic spectra for two different binding energies. Red line: full real-space calculation, green line: $k$-space "1s" excitonic basis. The pair continuum of the ordered case starts at energy zero

In order to substantiate this assessment, we also calculated the spectra by omitting the contributions from the continuum, see Fig. 11.

It is not possible to perform this calculation in the present tight-binding scheme. The continuum can be switched off by using the $k$-space model and projecting the optical polarization onto the lowest excitonic relative-motion states (called loosely "1s" here). Although it seems plausible, that the continuum influences the excitonic spectra in the disordered case as explained, it should be kept in mind, that in $k$-space we have to apply two approximations and it might be that different features of the spectra in the different models are not only due to the presence or absence of the continuum, but in addition due to these approximations.

### 1.5.3 Full width at half maximum

We expect a saturation of the width that is given by the total energetic width of the disorder potential. However, in Fig. 12 (upper row) we observe not only a single saturation value. It rather seems to depend on Coulomb strength. To clarify this point, we again look at the pure "1s" spectrum as obtained from the $k$-space approach in the way just explained. We see that now (Fig. 12, lower left) the dependence of the saturation of the FWHM with increasing length scale on the Coulomb strength is much weaker if compared to Fig. 12 upper left.

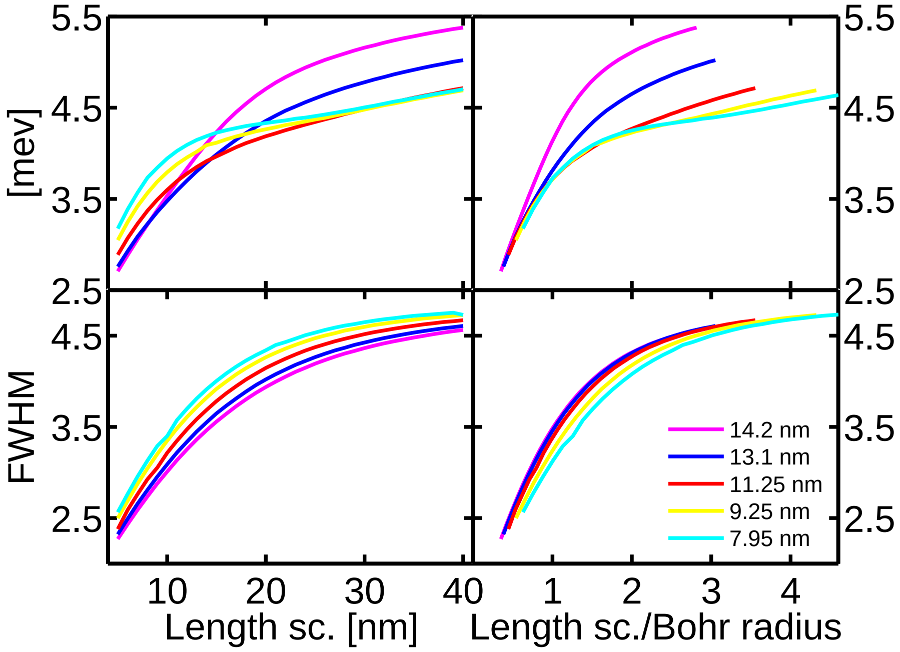

Figure 12: The full width at half maximum with real space calculation (upper row), and in $k$-space "1s"-excitonic basis (lower row) against the disorder length scale $L$ (left hand side) and $L/a_B$ (right hand side)

In addition, the order of the saturation values in Fig. 12 lower left is reversed with respect to that Fig. 12 upper left. The first observation indicates, that the continuum strongly influences the saturation width, in particular for small binding energy. The second observation can be understood as follows. For length scale smaller than Bohr radius it is known [13, 14] that the exciton relative motion averages over the disorder potential. For smaller binding energy the Bohr radius is larger than that for large binding energy. Thus, in the first case the exciton averages more efficiently over the disorder potential leading to a smaller effective amplitude if compared to the case of large binding energy. However, this averaging effect is fully active only for the case of comparable length scale $L$ and Bohr radius $a_B$, where the order of the curves in the left column in Fig. 12 agree. Without influence of the continuum (lower left figure in Fig. 12) this averaging effect may still contribute to larger $L$ as well.

The explanation of the monotonous increase with disorder length scale is the following: For length scale smaller than the Bohr radius the exciton thus sees always a reduced disorder amplitude with correlation length comparable to the Bohr radius. This reduced disorder strength leads to a reduced inhomogeneous width in this case. For a length scale much larger than the Bohr radius the Bohr radius does not directly influence the spectral width. It is clearly seen that the cross-over between these two regimes is close to the point where the disorder length scale equals the Bohr radius, Fig. 12.

### 1.5.4 Energy distribution vs. spectrum

In Fig. 13 the broken lines show the distributions of the local disorder potential for a given $W$ (after renormalization) and for different disorder length $L$. Note, that even for $L = 5$ nm the applied Gauss-filter leads to a deviation of the energy distribution from the input distribution, which is box-shaped. In addition, this figure also shows the two corresponding excitonic spectra (solid line).

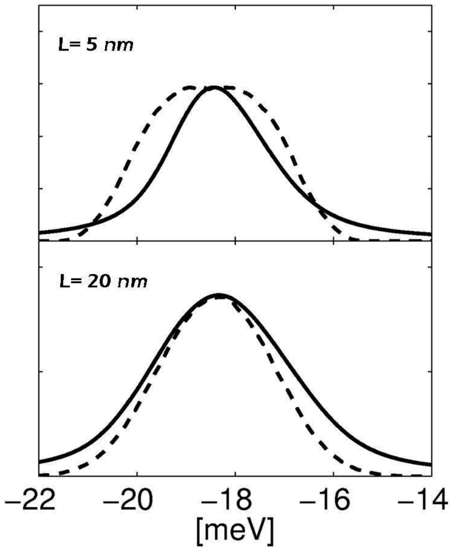

Figure 13: Site-energy distribution (broken line) and excitonic spectra (solid line) for two different $L$. The distributions are normalized to the excitonic spectra.

For small $L$ the excitonic spectrum is narrower, showing the above mentioned action of the averaging due to the relative motion. For large $L$ one expects equal width. However, the excitonic spectrum is calculated assuming a certain homogeneous width ($T_2$-time), which contributes to the total width.

This effect is underlying the monotonious increase of the widths with $L$.

### 1.5.5 Shift of the maximum

In order to see to what extent it is the pair continuum, which causes the shift of the spectral maximum, we look at the spectral features extracted from a "1s"-calculation. In the first row of Fig. 14 we see, that the red shift for increasing length scale is absent. However, it would be naive to say that the continuum alone produces the red shift. Remember that in the $k$-space model we have two additional approximations. They might lead to additional differences in the spectra.

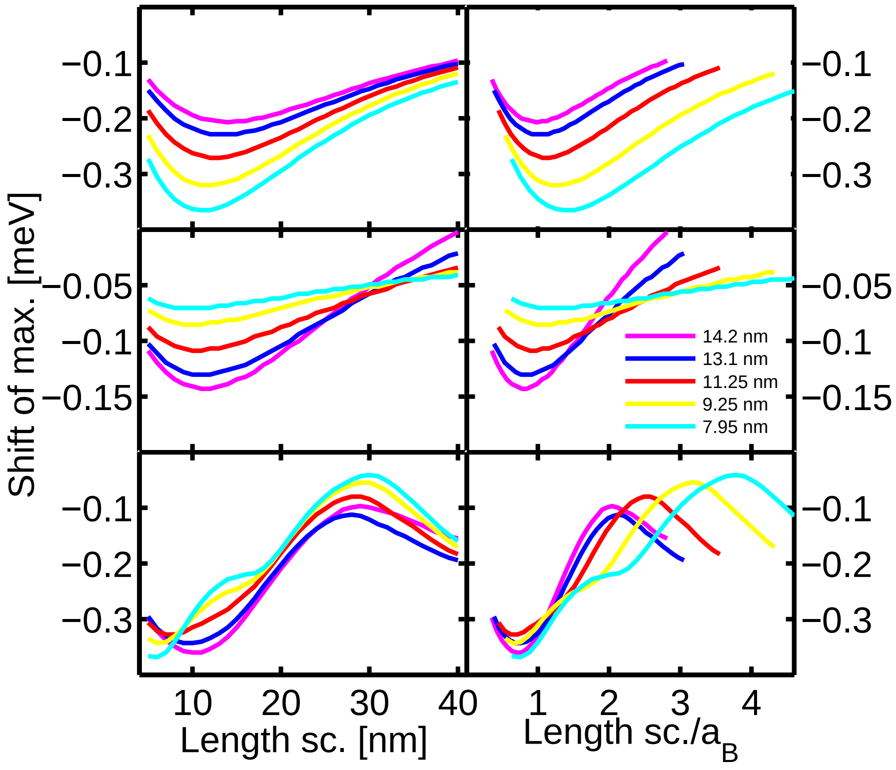

Figure 14: The shift of the maximum from calculation using different basis. First row: $k$-space "1s"-exciton basis, second row: k-space single particle basis, third row: real space model. Different colors correspond to different $a_B$

That this is reasonable can be seen comparing the curves for the shift for different Coulomb strength.

The question whether it is the two approximations or the continuum which lead to the different behavior of the shift at large length scale, can be clarified by repeating the $k$-space calculation, but instead of projecting the polarization onto the "1s"-excitonic relative motion state doing a full calculation where all excitonic states are included, i.e., also the pair continuum, see the second row of Fig. 14. Also here the red shift for large $L$ is absent. However, now the order of the different curves agrees, at least for $10$ nm $< L <$ $30$ nm, with that of the real-space model. On the other hand, for $L < a_B$ a different behavior persists. This shows, that it is not only the presence or absence of the continuum, which leads to deviations from the results of the real-space model, but also the two approximations in the $k$-space model have an influence on the finer details of the results.

For given Coulomb strength the initial red shift (by increasing $L$) is a well known feature of excitonic spectra [5,6,18] calculated from a disordered model with $L \leq a_B$. It results from the fact that for a disordered structure the line is asymmetric, having a more extended tail towards higher energies. If $L$ increases, the relative motion does no longer average the disorder potential sufficiently, such that the effective disorder amplitude increases and the line becomes wider. This leads to a more asymmetric shape and, concomitantly, also to a larger red shift. If $L$ is larger than $a_B$, the averaging becomes ineffective and the exciton follows the long-range disorder potential. Since this has a symmetric shape around its average value, the maximum returns to the position of the ordered case, leading to the blue shift. Ultimately, the shift should approach zero for $L \to \infty$. At present it is not quite clear to us, why the spectra calculated from the real-space model for further increasing length scale again show a red shift. It is to be noted, however, that this shift occurs at a very small energy scale.

By comparing the figures in Fig. 14 one realizes the following difference: The shift resulting from the real-space model (third row of Fig. 14) shows two different regimes. For $L \leq a_B$ there is no unique trend in the dependence on the Coulomb strength. By decreasing $a_B$ there is a non-monotonous behavior. For $L > a_B$ , on the other hand, the shift increases with increasing $a_B$. This is in accord with the result from the full $k$-space model. Only at very large $L$ there is a cross-over. In contrast, the $k$-space "1s"-model results in a reverse order. Here the largest shift occurs for the smallest $a_B$. This point is not understood at present. However, the tiny energy scale should be taken into account also here.

### 1.5.6 Excitons in a disordered environment

In order to understand the features of the spectra in more detail we have to keep in mind that the contributions to the inhomogeneous line are due to localized excitons. Here localization means that the center-of-mass (com) motion of the excitons is localized. In addition to this localization the contributions to the line are not only due to the excitonic “1s”-resonances distributed energetically and locally. As mentioned above, the center-of-mass $K$-selection rule valid in an ordered potential breaks down in the disordered environment. This selection rule prevents coupling of the light-filed to the com-continuum in the ordered case. Thus in addition to the lowest excitonic com-transition (the “1s”-resonance) also the excitonic com-continuum at higher energy contribute to the spectra. However, due to localization, this higher-energy transitions are not really represented by a continuum [35]. There is level-spacing due to lateral confinement as a consequence of localization. The characteristic energy of this spacing has been termed $E_{\mathbf{ref}}$ by Runge and Zimmermann [6] and contributes of the asymmetry of the excitonic line. Every excitonic contribution is therefore represented by a succession of lines. Their energetic separation depends on the disorder length scale $L$. Of course, the dominant contribution is still given by the lowest transition energy (which was the “1s”-transition at com $K = 0$ in ordered situation). In the configurationally averaged spectrum these lines then form a continuum extending towards higher energies.

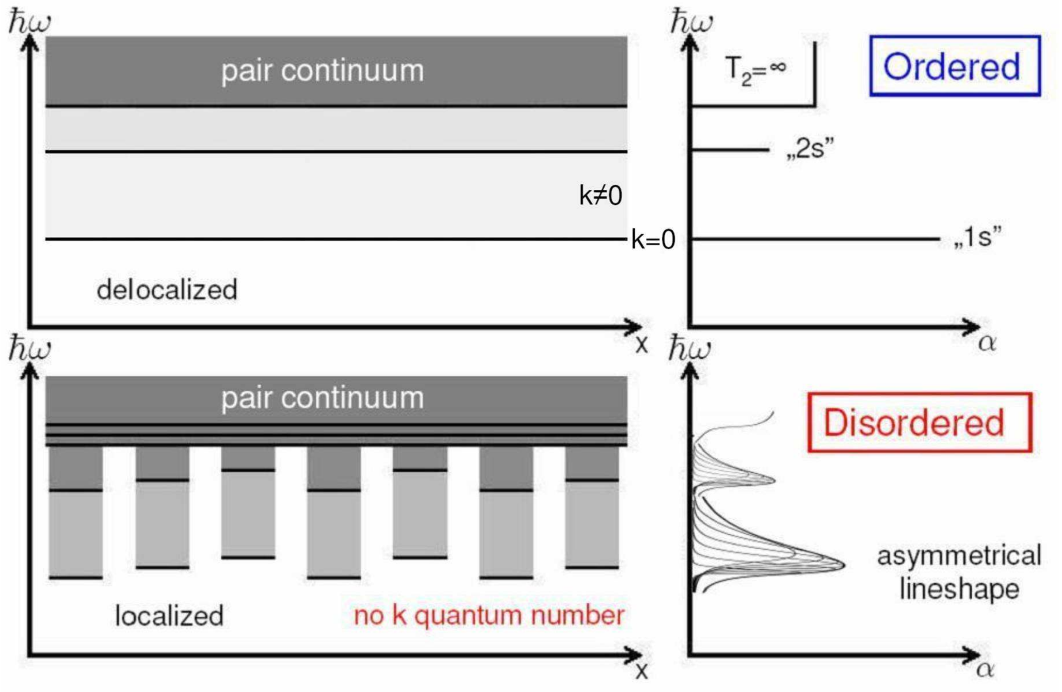

Figure 15: Schematic picture of the excitonic energies (left-hand figures) showing the center-of-mass continuum and the pair continuum, and the corresponding linear spectra without phenomenologically introduced dephasing in ordered (upper row) and disordered (lower row) case

The extension of the excitonic com-continuum towards higher energies depends on the length scales (and amplitude) of the disorder potential. As mentioned before, for very short-range potential the averaging effect of the relative motion produces a disorder potential with reduced amplitude [13]. This limits the shift. Increasing the length scale, but still below the Bohr radius, the averaging becomes less effective and the effective disorder potential increases, producing more center-of-mass excitonic states at lower energies. Thus a red shift appears. It is known (e.g. [5]), that the excitonic spectra in the disordered case always show a certain red shift if compared to the ordered case, [35].

For length scales larger than the Bohr radius the center-of-mass states follow the whole disorder landscape, occupying both low- and high-energy positions. Here it is important to realize that for a com-state in the lower part of the spectrum there is a reduced possibility to couple to com-states of neighboring excitons. This is due to the fact that the density of com-states is small in the low energy tail of the inhomogeneous spectrum. In contrast, for states in the center of the spectrum or at even higher energies coupling to the com-exitonic "continua" of neighboring localized excitons becomes possible. This mixing resembles a Fano-situation and will be studied in detail in the next Chapter.

## 1.6 Dependence of spectral width on hole mass

During the course of this work we received experimental data [36] on excitonic linewidths in a disordered semiconductor quantum-well structure. The spectrum consists of a heavy-hole and a higher lying light-hole peak. It is remarkable, that the inhomogeneous width of the light-hole exciton is much smaller than that of the heavy-hole one. In order to understand this feature the linear excitonic spectrum is studied for different hole masses on the basis of the real-space model.

The hole mass is determined by the valence-band coupling $J^v \propto (m^v)^{-1}$. The hole-mass enters the reduced excitonic mass, which in turn determines the Bohr-radius. As for larger Bohr-radius, i.e., for smaller reduced mass or larger $J^v \propto (m^v)^{-1}$, the averaging due to the relative electron-hole motion is more effective, we expect in fact, that for smaller hole mass the inhomogeneous width is smaller. However, in reality in a quantum well the disorder amplitude due to well-width fluctuations increases with decreasing mass of a particle, $W^v/J^v = const$. This effect counteracts the just mentioned averaging mechanism.

To clearly distinguish these two effects we first take the disorder amplitude to be independent of $J^v$, i.e., $W^v = const$. Fig. 16 shows the result for the width as a function of $J^v$ (dashed line). It is seen that for $L \leq a_B$ the width in fact decreases with increasing $J^v$, i.e., decreasing mass. For $L > a_B$, on the other hand, the width stays more or less constant, see Fig. 16, first row, right. We now take in addition the mass-dependence of the disorder amplitude into account. We then see that the averaging effect is counteracted. The result shows even the opposite trend, i.e, the

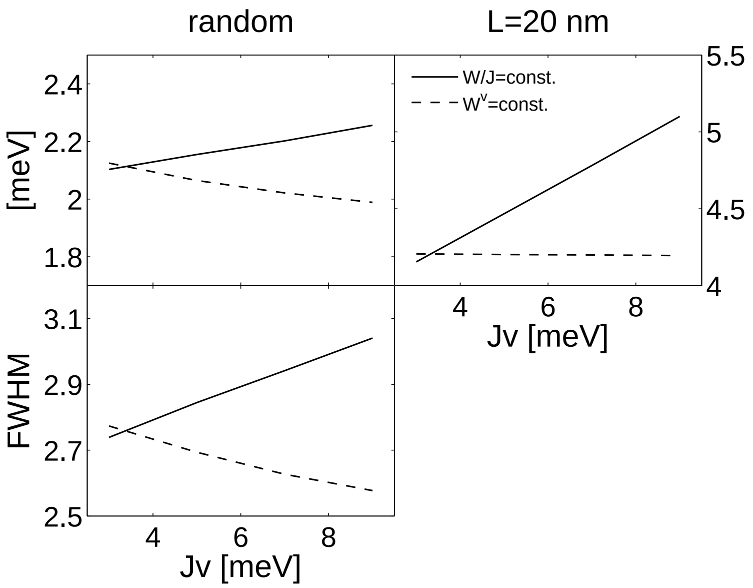

Figure 16: Full width at half maximum for different cases. Solid line correspond to the case when $W^v/J^v$ is constant, dashed line corresponds to the case when $W^v$ is constant, first row $W/J$=0.2, second row $W/J$=0.3, first column random energies, second column disorder with L=20 nm length scale

width increases with decreasing mass considerably.

Therefore, at least for the present model, based on disorder due to well-width fluctuations, it can not be stated that the smaller inhomogeneous width of the light-hole exciton, if compared to that of the heavy-hole one, is due to its smaller mass.

## 1.7 Summary of Chapter 1

In this Chapter the influence of the length scale of the disorder potential on the width and shift of the excitonic linear absorption peak was studied for different strength of the Coulomb interaction. Two different one-dimensional models have been used: a real-space tight-binding model and a $k$-space model. The latter includes two approximations (second-Born and Markov). In addition the quality of the second approach, if compared to the first one, which is free of approximations, had to be assessed.

The model calculations showed, that both width and shift are determined by $L/a_B$, if $L \leq a_B$, in an universal manner. For larger $L$ the Coulomb interaction did not directly influence the dependence of the spectral features on $L$. Details could be understood by invoking the averaging action of the relative electron-hole motion. In addition, the electron-hole pair continuum had some influence on these spectral features.

A limitation of the real-space model lies in the lattice constant, which is taken

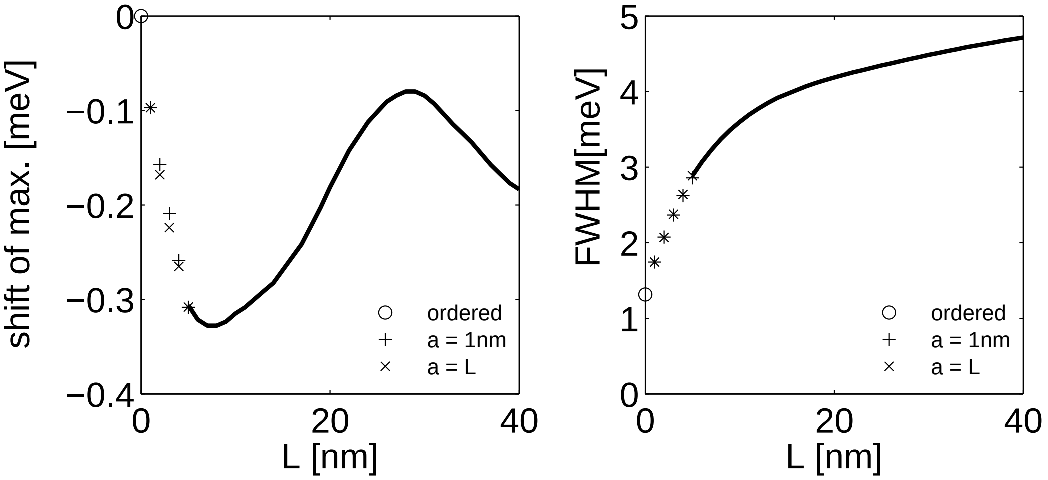

Figure 17: The length scale dependence of the shift of the maximum (left) and the FWHM (right) in case $a_B = 11.25$ nm complemented with calculation for smaller site separations

to be $a$=5 nm. In order to check the consistency of the calculation in real space, we studied the dependence of shift and width for even smaller $a$. This has been done using two different approaches. First, the lattice constant $a$ in the tight-binding model was set to be 1 nm. The Gauss-filter took care of length scales $L$ between 1 nm and 5 nm. The results are shown in Fig. 17 as $+$ signs. Alternatively, we adjusted $a$ to be equal to $L$ for 1 nm $\leq L \leq$ 5 nm. The results are shown in Fig. 17 as $\times$ signs. In both cases the couplings $J^c$ and $J^v$ and the disorder amplitudes $W^c$ and $W^v$ have been rescaled accordingly. Both methods yield nearly identical results.

It is seen that the width approaches 1.31 meV, which is the homogeneous width used as an input parameter. For decreasing $a$ the shift seemingly approaches zero which is the value of the ordered case. This once more reflects the averaging of the disorder potential due to the relative motion of electron and hole, which is in particular effective for small $L/a_B$.

As far as the quality of the $k$-space approach is concerned, one can state that, although the linear spectra look quite similar to each other, finer details do not agree. Therefore, one has to be cautious to use the $k$-space model, including the second Born and Markov approximations for a detailed study of optical properties of disordered semiconductor structures.

# 2 Nonlinear spectroscopy

In this Chapter the spectral features of excitonic excitations will be studied in more detail. These include various disorder-induced contributions to the inhomogeneous and homogeneous broadening, effects of localization and various couplings that become possible due to the break-down of the center-of-mass (com) $K$-selection rule, which holds in the ordered situation. To this end we have to go beyond the regime of linear response.

It is well known [18], that homogeneous and inhomogeneous contributions to the linewidth can not be distinguished in linear spectra. At least a third-order nonlinear experiment is required. In our case we concentrate on a variant of the Four-Wave-Mixing (FWM) technique, since there exist experimental data on semiconductor quantum wells [36]. These data have been analyzed already in terms of a simplified theory [15]. However, in that work the disorder was not treated on a microscopic basis, only a Gaussian convolution has been applied. Therefore, in this work, we apply our one-dimensional tight-binding model, including disorder in the sense of Chapter 1 to the calculation of the third-order optical response. In particular, we study the Two-Dimensional Fourier-Transform Spectra (2DFTS), which result from a double Fourier-transform of the temporal traces of the FWM signal [37].

This nonlinear technique not only gives detailed information about homogeneous and inhomogeneous broadening of spectral lines, it also enables us to identify various kinds of couplings that become possible in a disordered environment due to the relaxation of selection rules.

In the next sections a short summary of the most relevant equations is given and the 2DFTS method is explained in some detail. For more information about the theory of 2DFTS see [37].

Then the coupling, resulting from the break-down of the com-$K$-selection rule and from localization, will be studied in detail using 2DFTS. This coupling strongly reminds on a Fano-scenario [38]. Therefore, we first illustrate the features as seen in 2DFTS resulting from Fano-coupling in a simple level system. Then the disordered semiconductor model will be applied and it will be shown that in fact signatures of Fano-coupling can be identified in the 2DFT spectra. In addition, the notion of "disorder-induced dephasing" will be substantiated by these calculations.

In this Chapter we model the heavy-hole (hh) exciton in a disordered quantum well. We will consider co-circular excitation throughout. In this situation one sees, besides the hh-exciton resonance, induced absorption due to unbound two-exciton resonances at higher energies, while the bound biexcitonic features at lower energies are absent [37].

## 2.1 Nonlinear optics in the $\chi^{(3)}$ regime

In the following we analyze the third-order optical polarization. The model is still the one-dimensional tight-binding model of Chapter 1. The Hamiltonian of the system is also given above in Chapter 1.

The optical response up to the third order in the light field can be expressed using two transition-type quantities. These are the interband coherences

$$p_{ij} = \langle v_i^\dagger c_j \rangle, \tag{51}$$

i.e., single-exciton excitations, and

$$B_{mnij} = -\langle v_m^\dagger v_i^\dagger c_n c_j \rangle, \tag{52}$$

which describes two-exciton excitations. In order to be able to analyze correlation effects, it is advantageous to define

$$\bar{B}_{mnij} = B_{mnij} + p_{mj} p_{in} - p_{mn} p_{ij}. \tag{53}$$

The linear equation of motion reads

$$-i\hbar \frac{\partial}{\partial t} p_{ij} = -\sum_l T^c_{jl} p_{il} - \sum_k T^v_{ki} p_{kj} + V_{ij} p_{ij} + \mathbf{E}(t) \cdot \mathbf{d}^*_{vc}. \tag{54}$$

The second-order equation contains the two-exciton contribution

$$\begin{aligned} -i\hbar \frac{\partial}{\partial t} \bar{B}_{mnij} = &-\sum_k \left( T^c_{jk} \bar{B}_{mnik} + T^v_{ki} \bar{B}_{mnkj} + T^c_{nk} \bar{B}_{mkij} + T^v_{km} \bar{B}_{knij} \right) \\ &+ \left( V_{mn} + V_{mj} + V_{ni} + V_{ij} - V_{mi} - V_{nj} \right) \bar{B}_{mnij} \\ &- \left( V_{mn} + V_{ij} - V_{mi} - V_{nj} \right) p_{in} p_{mj} \\ &+ \left( V_{in} + V_{mj} - V_{mi} - V_{nj} \right) p_{mn} p_{ij}. \end{aligned} \tag{55}$$

Finally, the third-order polarization is determined by

$$\begin{aligned} -i\hbar \frac{\partial}{\partial t} p_{ij} = &-\sum_l T^c_{jl} p_{il} - \sum_k T^v_{ki} p_{kj} + V_{ij} p_{ij} \\ &+ \sum_{m,n} \left( V_{nj} - V_{ni} - V_{mj} + V_{mi} \right) p^*_{mn} \left( p_{mj} p_{in} - p_{mn} p_{ij} - \bar{B}_{mnij} \right) \\ &+ \mathbf{E}(t) \cdot \mathbf{d}^*_{vc} \left( 1 - \sum_{m,n} \left( p^*_{nm} p_{nj} + p^*_{mn} p_{in} \right) \right). \end{aligned} \tag{56}$$

The matrix $T^{c/v}_{ij}$ is the same as before, but the Coulomb matrix elements are now defined in a slightly different way, see Appendix B, without affecting the relevant results. The optical dipole matrix elements $\mathbf{d}^*_{vc}$ now are two-dimensional vectors that lead to the angular-momentum selection rules.

For a detailed discussion and application to more complex models, e.g., systems with more than just a single conduction and valence band, see [18].

## 2.2 Two-dimensional Fourier-transform spectroscopy

The 2DFT spectroscopy is based on a four-wave-mixing experiment. We consider the experimentally relevant situation where three short pulses excite the system, see Fig. 18. The envelope of the pulses is assumed to be given by a Gaussian characterized by a width $\delta$. As the amplitude of the pulses enters just as a trivial prefactor, we take them to be equal ($\eta_0$).

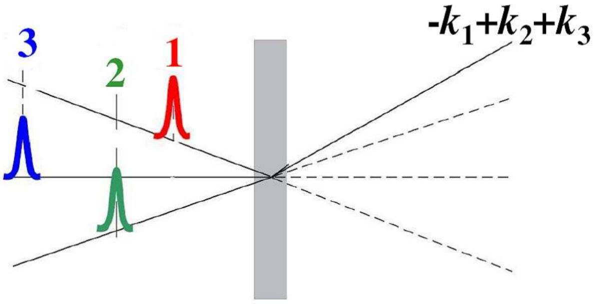

Figure 18: Scheme of a four-wave mixing experiment

The pulses propagate in directions $\mathbf{k}_1$, $\mathbf{k}_2$, $\mathbf{k}_3$, respectively. We study the outcoming light in the kinematic direction $-\mathbf{k}_1 + \mathbf{k}_2 + \mathbf{k}_3$. The first pulse (1) arrives at time $-\tau$ with $\tau > 0$, the second (2) at time $0$ and the last one (3) at time $T$. This mode is called the "rephasing mode".

$$\mathbf{E}_1(t) = \sigma \frac{1}{\sqrt{\pi\delta^2}} \eta_0 e^{-i\omega_L(t+\tau)} e^{i\mathbf{k}_1\mathbf{r}} e^{-(t+\tau)^2/\delta^2} \tag{57}$$

$$\mathbf{E}_2(t) = \sigma \frac{1}{\sqrt{\pi\delta^2}} \eta_0 e^{-i\omega_L t} e^{i\mathbf{k}_2\mathbf{r}} e^{-t^2/\delta^2} \tag{58}$$

$$\mathbf{E}_3(t) = \sigma \frac{1}{\sqrt{\pi\delta^2}} \eta_0 e^{-i\omega_L(t-T)} e^{i\mathbf{k}_3\mathbf{r}} e^{-(t-T)^2/\delta^2} \tag{59}$$

where $\sigma = (1, i)$ is the polarization vector for right-handed circular polarization of the light field.

The third order polarization $P^{(3)}$ depends on all three time parameters, but the $T$ delay time is kept fixed ($T = 0$) here. After the two Fourier transformations ($t \leftrightarrow \omega_t$ and $\tau \leftrightarrow \omega_\tau$) we can present the amplitude, the real-part and the imaginary part of the third order polarization in contour-plots. As experimental data usually show the electric field instead of the polarization, we multiply $P^{(3)}$ by the imaginary unit [37]. The horizontal axis is the emission energy, corresponding to the signal frequency $\omega_t$, and the vertical axis displays the excitation energy corresponding to the frequency $\omega_\tau$ related the delay time between the first and second pulses. As a convention, in the rephasing mode of the experiment, the two-dimensional spectrum is spanned by positive $\omega_t$ and negative $\omega_\tau$. The diagonal then extends from the upper-left corner towards the lower-right corner. Independent two-level resonances would appear on this diagonal [37]. In the following, if we talk about "higher" energies, we mean $\omega_t \to +\infty$ and $\omega_\tau \to -\infty$.

## 2.3 Fano-situation

In the typical Fano-situation [38] there is an optical transition from a certain ground state to a single discrete state and a transition from this ground state into a continuum of states. The optical transitions are given by an optical dipole matrix element $\mu_{ag}$ into the single discrete state and by a constant dipole matrix element $\mu_0$ into the continuum. We consider here an unstructured continuum with a constant density of states $\rho$. However, the discrete state and the continuum are not considered to be eigenstates.

There is coherent tunneling from the discrete excited state to the continuum of states. The parameter $w$ characterizes this coupling. The reciprocal lifetime of the excitation of the discrete resonance is then given by $\Gamma \propto w^2$. $\Gamma$ determines the linewidth of the Fano-line, which is purely homogeneous.

The system Hamiltonian can be written as

$$\begin{aligned} H = & \varepsilon_g v_g^\dagger v_g + \varepsilon_a c_a^\dagger c_a + \sum_j \varepsilon_j c_j^\dagger c_j \\ & + \mu_{ag} E(t)(c_a^\dagger v_g + v_g^\dagger c_a) + \mu_0 E(t) \sum_j (c_j^\dagger v_g + v_g^\dagger c_j) \\ & + w \sum_j (c_a^\dagger c_j + c_j^\dagger c_a). \end{aligned} \tag{60}$$

In the first row of Eq. (60) the terms describe the kinetic contributions of the ground state $|g\rangle$ , the single state $|a\rangle$, and the continuum states $|j\rangle$. In the second row the interaction with the light field appears. The first term is the single state excitation, the second one is the excitation of the continuum. The last term (third row in the Hamiltonian) describes the coupling between the single state and the continuum with the coupling matrix element $w$, where $\Gamma = 2\pi w^2 \rho$ is valid [38]. The excitation

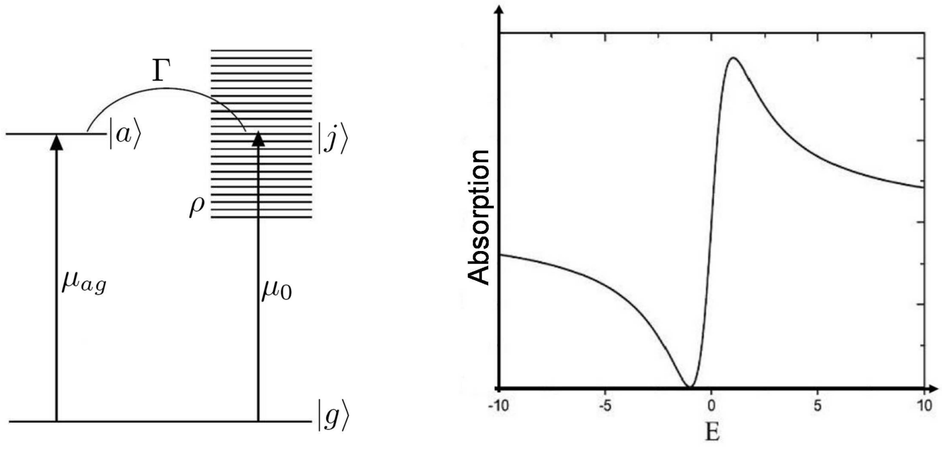

(a) (b)

Figure 19: Fano model (a) with the linear spectrum (b). Here $E = \frac{\hbar\omega - E_a}{\Gamma/2}$

pulses are represented in this tutorial case by

$$\begin{aligned} E_1(t) &= \eta_0 \delta(t+\tau) && (61) \\ E_2(t) &= \eta_0 \delta(t). && (62) \end{aligned}$$

The first pulse arrives at $t = -\tau$, with $\tau > 0$, the second and the third at $t = 0$. We look at the signal direction $2\mathbf{k}_2 - \mathbf{k}_1$

**Linear spectrum of the Fano situation**

The absorption spectrum is calculated from the linear polarization [18,38]

$$P^{(1)}(t) = -\frac{i\eta_0}{\hbar}\Theta(t)\rho\mu_0^2\left(2\pi\delta(t) + L(t)\right), \tag{63}$$

where

$$L(t) = \pi\frac{\Gamma}{2}(q-i)^2 e^{-iE_a t - \frac{\Gamma}{2}t}, \tag{64}$$

showing the contribution of the continuum $2\pi\delta(t)$ and the discrete state contribution $L(t)$ including the coupling $\Gamma$. Here

$$q = \left(\frac{2}{\pi\Gamma\rho}\right)^{1/2}\frac{\mu_{ag}}{\mu_0} \tag{65}$$

is the Fano-parameter.

The Fourier -transform of $P(t)$ is

$$P^{(1)}(\omega) = -\frac{i\eta_0}{\hbar}\rho\mu_0^2\left(1 + \frac{\frac{\Gamma}{2}(q-i)^2}{\frac{\Gamma}{2} - i(\hbar\omega - E_a)}\right). \tag{66}$$

Its imaginary part gives the linear spectrum shown in Fig. 19(b).

Because of the interference between the two excitation paths via the discrete state and the direct continuum excitation the resulting line shape is not simply a superposition of a Lorentzian and an unstructured continuum, see Fig 19. The resulting line is asymmetrical, showing zero absorption at an energy close to the discrete resonance.

### Third-order polarization for the Fano situation

The third-order polarization can be calculated in this simple level model in terms of the first-order polarizations as follows [18]

$$P^{(3)}(t,\tau) = 2\frac{i\eta_0}{\hbar}P^{(1)}(t)P^{(1)*}(\tau), \tag{67}$$

where $\tau > 0$. The Fourier transform provides

$$P^{(3)}(\omega_t,\omega_\tau) = 2\frac{i\eta_0^3}{\hbar^3}\rho^2\mu_0^4\left(1 + \frac{\frac{\Gamma}{2}(q-i)^2}{\frac{\Gamma}{2} - i(\hbar\omega_t - E_a)}\right)\left(1 + \frac{\frac{\Gamma}{2}(q+i)^2}{\frac{\Gamma}{2} + i(\hbar\omega_\tau - E_a)}\right) \tag{68}$$

In order to achieve an understanding of the spectral features that originate from a typical Fano situation in 2DFTS, we here present in a step-by-step way the evolution of the final Fano-2DFT spectrum.

### 2.3.1 Towards the 2DFTS of the Fano-situation, Step 1)

Let us start with a single transition, which we give a certain small phenomenological dephasing rate $\gamma$. As seen in Fig. 20 we obtain a peak (red=maximum, blue= minimum) in the amplitude 2DFTS. The cross-like structure is a trivial result of the combination of the two Fourier-transformations. This spectrum is just the two-dimensional plot of

$$P^{(3)}(\omega_t,\omega_\tau) = 2\frac{i\eta_0^3}{\hbar^3}\mu_{ag}^4\left(\frac{1/\pi}{\gamma - i(\hbar\omega_t - E_a)}\right)\left(\frac{1/\pi}{\gamma + i(\hbar\omega_\tau - E_a)}\right) \tag{69}$$

which results from Eq. (68) if we take $\Gamma \to 0$ and $\mu_0 \to 0$.

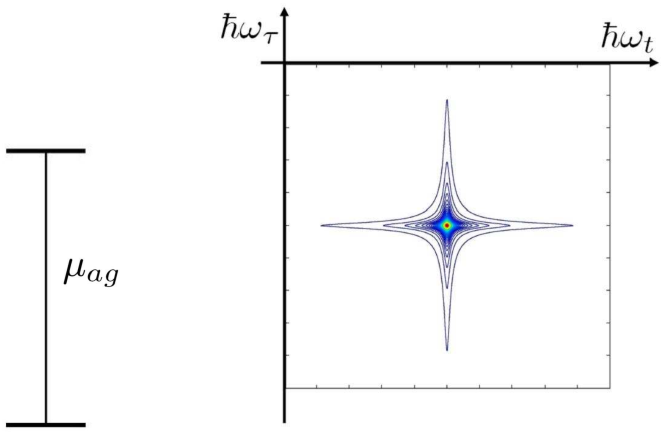

(a) (b)

Figure 20: Two-level absorber (a) with its 2DFT spectrum (b)

### 2.3.2 Towards the 2DFTS of the Fano-situation, Step $2)$

Consider now an ensemble of uncoupled TLS (two-level system) with random transition energies $E_i$, see Fig. 21. This would simply yield peaks along the diagonal in the 2DTF spectrum, corresponding to the different transition energies $E_i$.

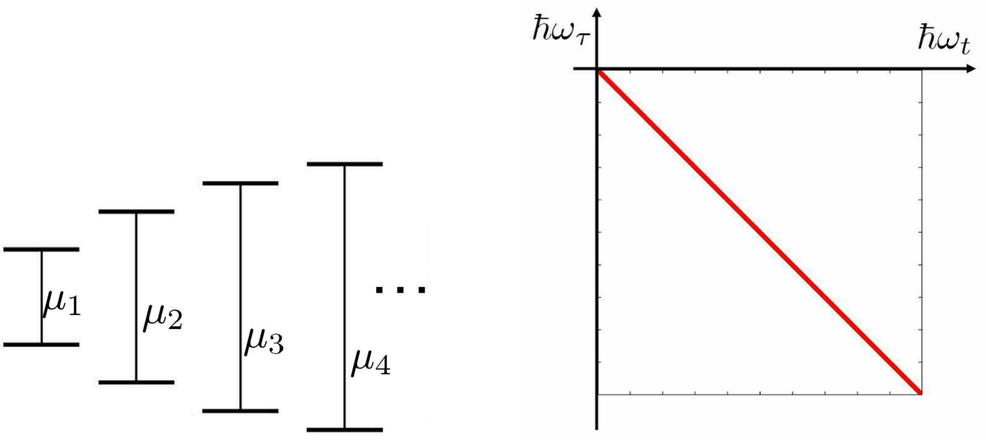

(a) (b)

Figure 21: Uncoupled two-level absorbers. Here no dephasing is assumed. Otherwise the line would be broadened parallel to the diagonal

### 2.3.3 Towards the 2DFTS of the Fano-situation, Step $3)$

However, the situation becomes completely different, if we consider an ensemble of transitions that are coupled by light to just one single and thus common ground state, see Fig. 22. From Eq. (68) we obtain for $\Gamma \to 0$ and $\mu_{ag} \to 0$

$$P^{(3)}(\omega_t, \omega_\tau) = 2\frac{i\eta_0^3}{\hbar^3}\rho^2\mu_0^4, \tag{70}$$

i.e., a constant value for all $\omega_t$ and $\omega_\tau$ pairs, provided the density of states and the optical matrix elements are taken to be constant (unstructured continuum).

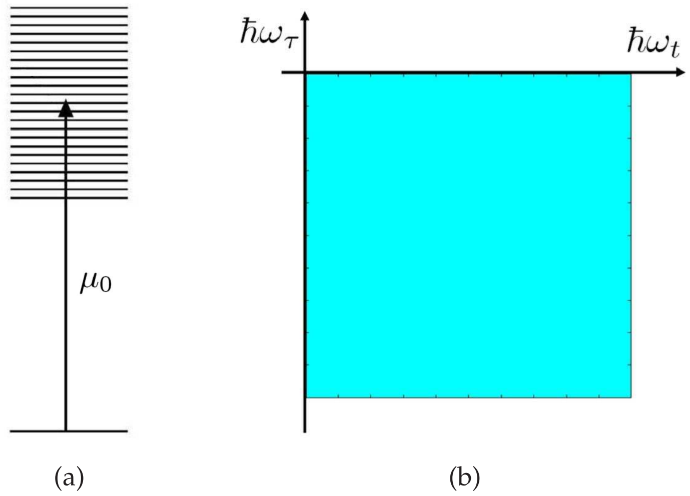

Figure 22: 2DFT spectrum for an unstructured continuum. It does not have a lower or upper bound within the energy window of (b)

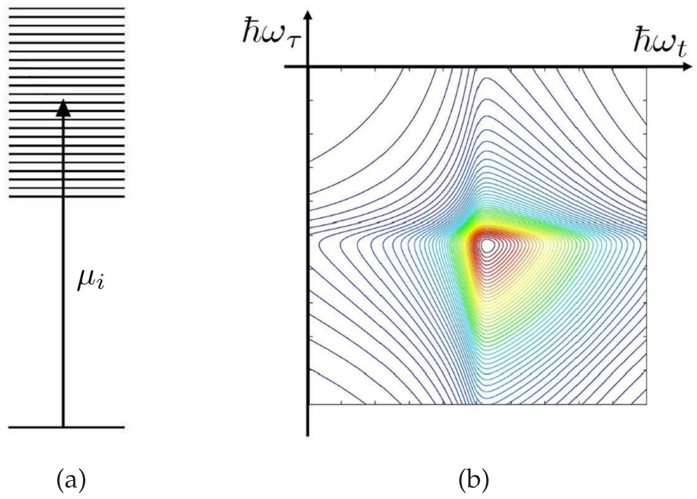

Figure 23: 2DFT spectrum for a continuum with optical dipole matrix elements decaying towards higher energies in a Gaussian manner

For later reference we also present here the 2DFT spectrum for a certain structured continuum. We consider a lower bond of the transition energies which lies in the energy window of the 2DFT spectrum In addition, we take the optical dipole matrix elements $\mu_i$ to decay in a Gaussian manner towards higher energies, the lowest transition being the strongest, see Fig. 23. It is now seen, that there are two strong arms extending from the lowest energy at the diagonal towards both higher $\omega_t$ and -$\omega_\tau$. In the area in the lower-right corner of the spectrum there is a decaying, but otherwise unstructured contribution.

### 2.3.4 Towards the 2DFTS of the Fano-situation, Step $4)$

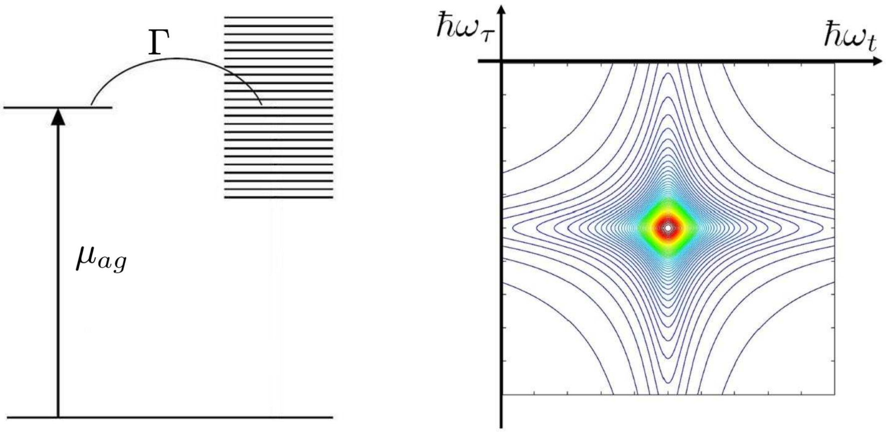

(a) (b)

Figure 24: Fano situation without continuum-excitation

We now consider a transition into the discrete state with dipole matrix element $\mu_{ag}$, which is coupled by $w$ (i.e., the decay rate is given by $\Gamma$) to the non-excited continuum, see Fig. 24. The 2DFT spectrum is then given by Eq. (68) with $\mu_0 \to 0$:

$$P^{(3)}(\omega_t, \omega_\tau) = 2\frac{i\eta_0^3}{\hbar^3}\mu_{ag}^4 \left(\frac{1/\pi}{\frac{\Gamma}{2} - i(\hbar\omega_t - E_a)}\right)\left(\frac{1/\pi}{\frac{\Gamma}{2} + i(\hbar\omega_\tau - E_a)}\right). \tag{71}$$

It therefore resembles the pattern seen in Fig. 20 for the two-level system. However, instead of the phenomenological dephasing rate $\gamma$ the homogeneous width is now determined by the coupling of the discrete state into the continuum.

### 2.3.5 Towards the 2DFTS of the Fano-situation, Step $5)$

Now we look at a single-state transition and an excited continuum. The single state is optically coupled to the continuum via the ground state, but there is no tunneling between them. The linear spectrum is then given by a superposition of the spectral line of the single state and the spectrum of the continuum. In other words, the spectrum of the single transition is just sitting on top of the continuum. The same feature can also be seen in the 2DFT spectrum, see Fig. 25. The crosses now extend (for an unstructured continuum) without decay towards higher and lower energies. They reflect the optical coupling of the single state to the continuum via the ground state ($\Gamma \to 0$). The spectrum is now given by

$$P^{(3)}(\omega_t, \omega_\tau) = 2\frac{i\eta_0^3}{\hbar^3}\rho^2\mu_0^4 \left(1 + \frac{\mu_{ag}^2/(\pi\rho\mu_0^2)}{\gamma - i(\hbar\omega_t - E_a)}\right)\left(1 + \frac{\mu_{ag}^2/(\pi\rho\mu_0^2)}{\gamma + i(\hbar\omega_\tau - E_a)}\right), \qquad (72)$$

where a phenomenological $\gamma$ has been introduced.

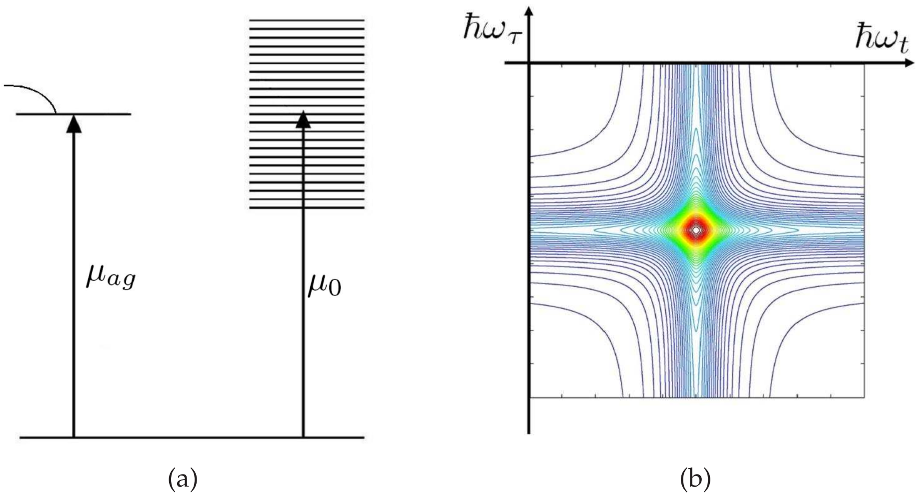

(a) (b)

Figure 25: Fano situation without coherent tunneling

### 2.3.6 Fano-situation, Step 6)

As has been mentioned before, the tunneling between the single state and the continuum leads to an asymmetric line shape of the linear spectrum. The 2DFT spectrum also shows this asymmetrical feature, see Fig. 26. It is now given by Eq. (68). The peak is slightly shifted compared to the case before, and the right-hand and down arms are stronger compared to the upper and left-hand arms. It has to be noted that here no phenomenological dephasing $\gamma$ has been introduced into the calculation. The (homogeneous) linewidth is purely due to the coupling to the continuum.

As mentioned above the homogeneous linewidth can be determined within the 2DFTS scheme by looking at a spectrum (real or imaginary part) that shows a dispersive feature. The homogeneous linewidth, and therefore the reciprocal dephasing time $T_2$ is then given by the energetic distance between the maximum and the minimum in a line perpendicular to the diagonal. If this scheme is applied to the present situation, we can describe the line as being characterized by an effective dephasing rate that depends on transition energy $\hbar\omega$, i.e., by $T_2(\hbar\omega)$. It should be noted

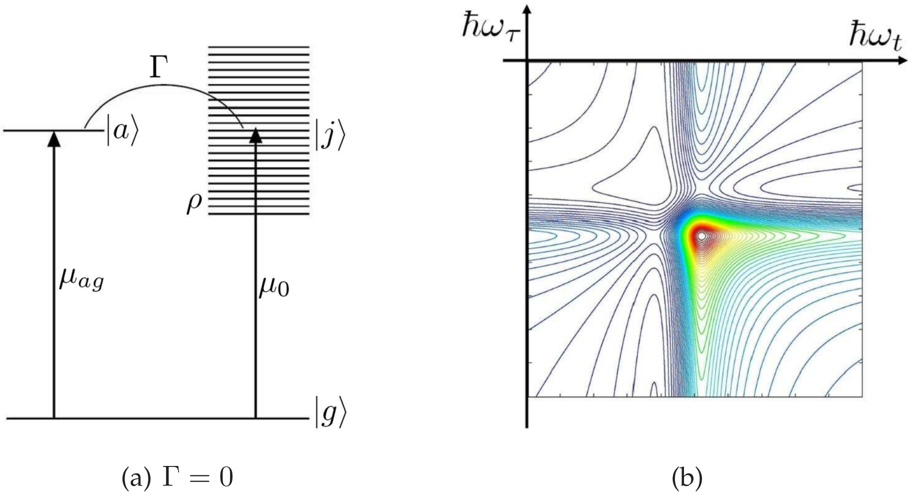

(a) $\Gamma = 0$ (b)

Figure 26: Full Fano situation

that this effective dephasing is not built into the model as a phenomenological rate but rather originates from the coupling into a continuum.

We will return to this observation when we discuss the 2DFT spectra of our disordered semiconductor model below.

## 2.4 2DFTS calculation for the disordered semiconductor model

### 2.4.1 The model parameters

After this preparation we are now in a position to present and discuss our results obtained for the 1-dimensional tight-binding model of a disordered semiconductor. Here we use the following model parameters: Number of sites $N = 10$, number of realizations $M = 40$, site separation $a = 5$ nm, intraband coupling for electron $J^c = 22.9$ meV and for holes $J^v = 3.338$ meV, disorder parameter $W/J = 0.2$, length scale $L = 12$nm, Bohr radius $a_B \approx 12$ nm (resulting from the Coulomb strength $V_0$, the regularization parameter $a_0$, and the couplings, see Appendix B).

We will be interested in the spectral features of the two-dimensional spectrum which show us the influence of disorder on homogeneous and inhomogeneous broadening and allow us to determine the various broadening parameters quantitatively. This knowledge will in the future be useful if experimental 2DFTS data will be available for semiconductor heterostructures that are characterized by a certain disorder.

### 2.4.2 A typical result for the heavy-hole exciton

In Fig. 27 we show an amplitude spectrum for the model with the above parameters. We see a dominant excitonic peak (the "1s"-peak). In the figure it appears at

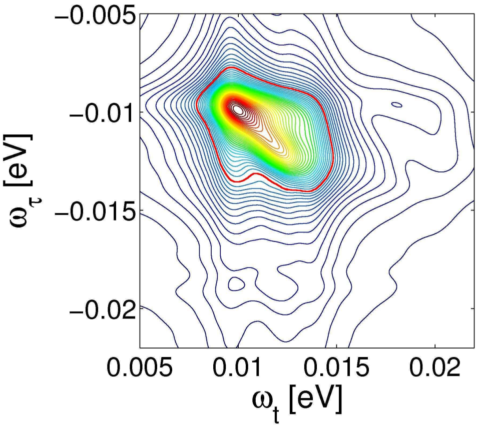

Figure 27: Heavy hole excitonic resonance in amplitude 2DFTS of the disordered semiconductor model. The red line is a guide to eye

0.011 eV and the pair continuum starts at energy 0.03 eV, i.e., outside the spectral window of Fig. 27, so the binding energy is 19 meV.

Along the diagonal towards higher energies there is a continuous decay in amplitude. This roughly resembles the decay of the linear spectrum at energies above the “1s”-peak. Towards lower energies the decay is much faster, reflecting the asymmetric linear line shape of an exciton in a disordered environment.

In addition to these features, which already are known from the linear spectrum (see Chapter 1), we realize additional structures in the 2DFT spectrum, which yield further information about the action of disorder on excitonic transitions. This information obviously cannot be deduced from a linear spectrum.

Extending from the “1s”-maximum there is a cross-like structure. Although such structure already appears for a single homogeneously broadened transition (see 2.3.1 above), here the four arms do not have equal strength. It can be seen that, in particular, the arms extending towards both higher $\omega_t$ and $\omega_\tau$ are stronger if compared to those extending towards lower energies. This reflects the Fano-like coupling discussed in 2.3.6 above.

Of course, we cannot exclude that this feature is due to a mechanism discussed in 2.3.3 for a structured continuum, where the strongest transition at the lowest energy is followed by weaker transitions to a continuum extending towards higher energies.

If the Fano-like scenario applies, we can interpret the mechanism leading to this spectral feature in terms of the coupling of a given localized exciton to the comcontinuum of a neighboring exciton. The second interpretation does not need coupling between different neighboring excitons, but applies already for a given exciton, where the lowest ("1s"-) transition is optically coupled to the com-continuum of the same exciton.

At present it is not possible to decide which of the two mechanisms applies to the given spectrum. In a Fano-like scenario one would expect to see a depression along the diagonal towards lower energies. However, for our present model we have a superposition of more than just one single excitonic peak due to the inhomogeneous broadening, which washes out this depression.

It is also seen, that along cuts that extend perpendicular to the diagonal the linewidth seems to increase with increasing energy. This reflects homogeneous broadening, that is not uniform for all energies. We come back to this point in 2.4.6.

### 2.4.3 Two-exciton contribution

The spectrum is clearly not symmetric with respect to the diagonal. This is due to the fact that for the excitation conditions treated here, namely co-circular excitation pulses, we have two-exciton contributions just above the excitonic main peak [20, 37] which result from induced absorption into unbound two-exciton states. Bound biexcitons are not excited in this experimental situation.

We have performed calculations where the two-exciton contributions have been completely omitted, case i). This results from a calculation in the Pauli-blocking limit. We have also applied a calculation, case ii), where the correlations beyond Hartree-Fock have been assigned a larger dephasing rate, which reduces the two-exciton contributions.

These results are shown in Fig. 28. Here the cases i) (first column), ii) (second column), and the full calculation (third column) are depicted. It is seen, that if we switch off the two-exciton contributions the spectrum indeed becomes symmetric with respect to the diagonal. The disorder-induced features, on the other hand, prevail.

### 2.4.4 Homogeneous broadening

In order to extract broadening parameters we follow the procedure described in [15]. In addition to the amplitude spectra (lowest row in Fig. 28) also the real-part (uppermost row) and imaginary-part (middle row) spectra are given. Here we concentrate on homogeneous broadening. The inhomogeneous plus homogeneous broadening can roughly be read off from the extension along the diagonal in the rephasing mode. The homogeneous broadening follows most clearly from the energetic distance between the maximum and the minimum along a line perpendicular to the diagonal in a spectrum, that shows dispersive features.

From earlier calculations [15,20,37] we know, that the hh-exciton, which we have

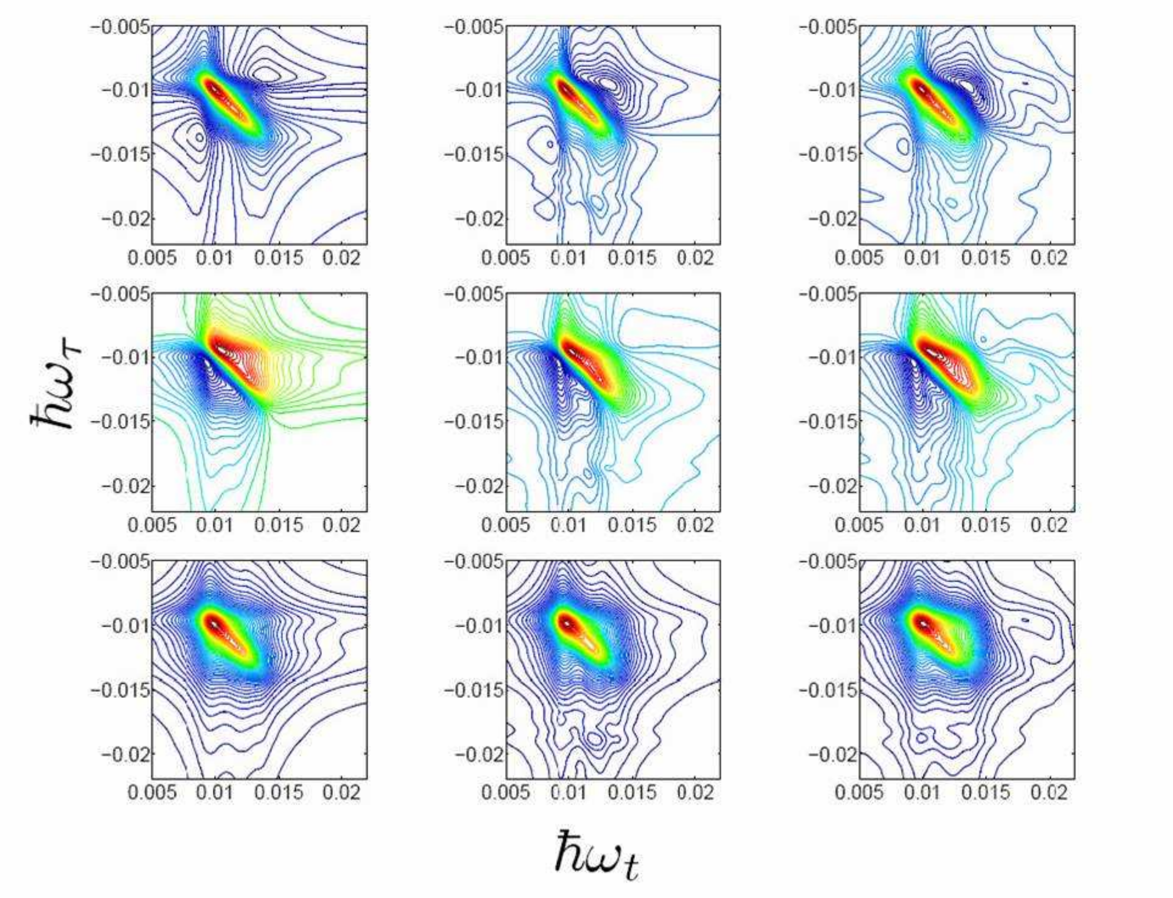

Figure 28: Heavy-hole excitonic resonance. First row - real part, second row - imaginary part, third row - amplitude spectra. First column - Pauli blocking, second column - increased two-exciton dephasing, third column - full calculation.

in mind exclusively here, shows a dispersive 2DFT spectrum if we look at the imaginary part (middle row in Fig. 28).

The full calculation (last figure in the middle row) already shows that we have a fan-like structure which could be interpreted as being due to an energy-dependent dephasing in the sense described above. The same feature, however, now symmetrically with respect to the diagonal, is seen in the results where the two-exciton contributions have been suppressed or excluded.

### 2.4.5 Disorder induced dephasing

In Fig. 29(b) the imaginary 2DFTS in the Pauli-blocking limit is shown for the disordered case together with the corresponding spectrum (full calculation) for the ordered case (a). The asymmetry in the disordered case is in clear contrast to the symmetric shape of the ordered case, even for the full calculation where the two-exciton resonances are not suppressed. Let us concentrate on homogeneous broadening deduced from the global maximum and global minimum in the imaginary-part spectra. We obtain a value of $\hbar/T_2 = 1.5$ meV of the disordered case. This value is by 20% larger if compared to the homogeneous broadening of the ordered case, see Fig. 29.

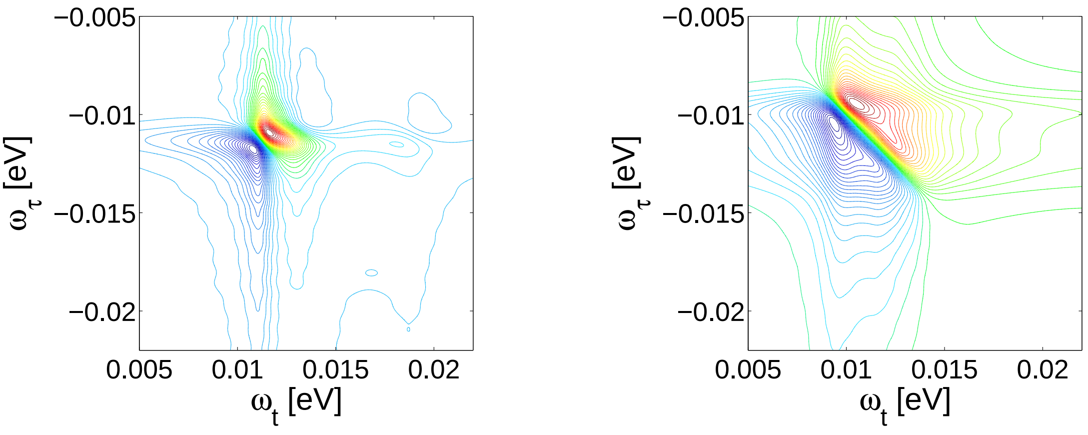

(a)

(b)

Figure 29: Heavy-hole 2DFTS (a) for the ordered case (full calculation), and (b) for the disordered case (Pauli-blocking limit)

This result can be taken as a substantiation of the previously introduced notion of “disorder-induced” dephasing [1–3]. In the first work [1], where a noninteracting model has been treated, it has been argued, that an optical coupling between a given ground state and a continuum leads to a broadening that should be interpreted as homogeneous broadening (see also [18]). It can not be rephased as a purely inhomogeneous line, which would lead to photon echoes, it rather leads to a decay of both the time-resolved and time-integrated traces in a conventional FWM-experiment. Such coupling becomes possible in a disordered environment due to the relaxation of the $k$-selection rule for single particle states in this model. In our present calculation the many-particle interaction has been included. As explained above, also in this case a selection rule is violated due to disorder. But this is now the $K$-selection rule for the com-states. In the ordered situation the com-continuum states have finite $K$ and do not optically couple to the ground state, while in the disordered situation they do. Thus there is the possibility for spectral features that are either due to a mechanism explained in 2.3.3 or in 2.3.6.

### 2.4.6 Energy-dependent dephasing

In Fig. 30 we show an enlarged portion of the imaginary-part spectrum resulting from a Pauli-blocking calculation. This situation has been chosen here in order to present the pure disorder-induced spectral features that are not disturbed by two-exciton contributions.

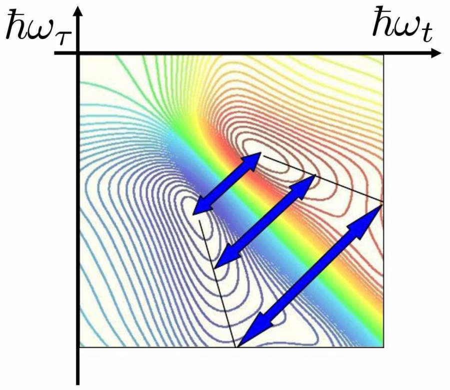

Figure 30: Imaginary hh-exciton 2DFTS showing energy dependent homogeneous broadening

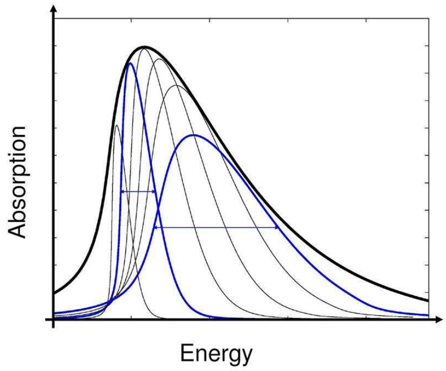

Figure 31: Line structure caused by both homogeneous and inhomogeneous broadening

In Fig. 30 the arrows indicate the energetic distance between minima and maxima along cuts perpendicular to the diagonal. These distances quantify the homogeneous broadening that depends on transition energy within the given line.

In Fig. 31 an interpretation is given schematically for the linear spectrum. The linear spectrum is here shown to be composed from excitonic lines that represent the inhomogeneous character of the total line. However, the individual homogeneous line widths are taken to be different.

While at energies below the central maximum the homogeneous line width is small, it increases for transitions at higher energies. Note, that in this schematical figure we have depicted the individual lines not as Fano lines with a characteristic dip below the main peak. In the superposition of these lines such dips would not show up. On the other hand, we have plotted the individual lines as asymmetric lines, which follow from the fact that not only a “1s”-transition couples to light, but also the com-transition at higher energies. The line shape of the individual lines is purely homogeneous, as explained in detail above. In addition, we have indicated the higher-lying lines to be broader. This reflects the increased possibility for a localized exciton with higher “1s”-transition energy to couple to the com-continuum of its local neighbors. This leads to the Fano-scenario.

The total line is, therefore, composed from individual, asymmetric homogeneously broadened lines with homogeneous width increasing with transition energy.

Note, that already the energetically lowest transition will have a homogeneous linewidth that is induced by disorder, since here the coupling to its own com-continuum produces a contribution to the homogeneous width.

## 2.5 Summary of Chapter 2

In previous work 2DFT spectra for a 1-dimensional disordered tight-binding model have been calculated [15]. However, instead of treating the disorder microscopically as in the present work, where the energies of the sites are randomly distributed in some way, in [15] spectra for the ordered case have been calculated and simply convoluted with a Gaussian, which resembles the inhomogeneous width. For the purpose of that work this approach was sufficient. It was intended to illustrate how one can determine homogeneous and inhomogeneous broadening of excitonic spectra of disordered semiconductor structures form 2DFT experiments performed in both the rephasing and nonrephasing modes.

However, the resulting spectra of this former approach are unable to show any traces of disorder-induced dephasing, asymmetrical lines and other features due to disorder. It was only shown that and how the phenomenologically introduced homogeneous and inhomogeneous broadenings could be determined from the spectra.

In the present work, on the other hand, we instead are able to study disorder induced features in detail.

Disorder not only localizes excitons in systems of reduced dimensionality but also breaks the $K$-selection rule and thus leads to additional coupling not present in the ordered counterpart. It is explained that this coupling can lead to a Fano-scenario. We have illustrated on the basis of a simple level system what kind of spectral features one can expect to be seen in 2DFTS for a Fano-situation. Extending from the main resonance, modeling here the heavy-hole exciton transition, a typical asymmetric feature is seen. This feature also results from calculations for the disordered semiconductor model. However, it is argued, that one can not easily differentiate between two different cases: i) the features result from just a given localized exciton and these spectra, reflecting eigenstates, are superimposed in the self-averaging experiment as is considered here, or ii) localized excitons couple to neighboring ones leading to the conventional Fano situation.

In any case it has been demonstrated that the overall homogeneous broadening of the disordered case is larger than that of its ordered counterpart by about 20% for the weak disorder considered. This substantiates the notion of “disorder-induced dephasing” for cases with comparatively weak disorder. In addition, applying a recently proposed scheme to determine homogeneous broadening from 2DFTS of disordered semiconductors we have seen that the spectra can be interpreted as being composed from contributions (within the inhomogeneous ensemble) that have energy-dependent dephasing rates, i.e., the rates increase with increasing energy. It is explained that this feature is due to coupling within a local excitonic system or between neighboring excitons.

# Summary and outlook

In this work two problems have been addressed. We first compared two different approaches for the calculation of optical properties of disordered semiconductors. It is shown that the equation of motion approach in $k$-space, formulated for the configurationally averaged linear optical polarization and including the second-Born and Markov approximations, leads to results that partly disagree with those obtained for the same model from a tight-binding real-space approach. It should be noted in passing that R. Zimmermann pointed out [29] that instead of the second Born approximation one should rather use the Coherent Potential Approximation (CPA) which does not lead to unphysical spectra. However, for the time being it is not clear to us how to implement this approximation in calculations of nonlinear optical properties. For the rest of this work we therefore apply the tight-binding real-space approach with subsequent configurational averaging, although it is much more demanding numerically if compared to the $k$-space approach.

The second problem focused on disorder-induced features of linear and nonlinear optical spectra. The influence of the length scale of disorder on shift and width of linear spectra of excitons was studied for the case of weak disorder. The results are interpreted in terms of the averaging of the disorder potential due to the relative motion of electrons and holes. This averaging mechanism is well known, however, its action for different length scales has not been studied in sufficient detail so far. We find that for length scale smaller than the Bohr radius there is a universal behavior, while for larger length scale the Coulomb interaction does no longer play a direct role.

We then focused on nonlinear 2DFT spectra. It was argued that in a disordered semiconductor various couplings (in the sense of Fano-couplings) become possible which are absent in the ordered counterpart. Modeling these couplings by a simple level model we showed in a tutorial manner how one can identify these couplings in 2DFT spectra. The calculation for the semiconductor model indeed showed features that closely resemble those found for the level system. It is therefore shown that in a disordered semiconductor Fano-like couplings are existing. They lead to disorder-induced dephasing and an interpretation of the excitonic line in terms of an energy dependent dephasing rate. It is also shown that two-exciton states obscure the spectra. It is therefore important to use such excitation conditions that do not yield large bi- or two-exciton contributions to the nonlinear response if disorder effects on the exciton are to be studied. We suggest to apply co-circular excitation for studies on disordered semiconductor structures.

Further work should be done in this field both experimentally and theoretically.

On the experimental side we would like to see 2DFT spectra for quantum wells that are characterized by disorder with different length scale. Preparation techniques exist that produce such samples. It would also be interesting to study the effect of disorder on bi- and two-exciton transitions in the 2DFTS scheme. There is some older work on Four-Wave-Mixing [40] which showed disorder effects of biexcitons. However, with 2DFTS we would expect much more information, in particular, for weak disorder. From previous work [15] we learned that in this case FWM in the time domain is more problematic to interpret.

In parallel, on the theoretical side, one should study in detail disorder broadening for situations where there are both heavy-hole and light-hole excitons which, depending on polarization of the excitation pulses, do or do not couple, at least within the Hartree-Fock limit. This coupling, however, is present in the ordered case due to correlations [20, 37], even if it is absent in the HF-limit. Disorder adds to the coupling scenario. Work is under way [39] that will certainly give interesting insights into these more complex structures. Experimental data exist that seem to show that both homogeneous and inhomogeneous broadenings of the two different excitons differ appreciably. An explanation for this finding does not yet exist.

Disorder effects on biexcitons would be another interesting problem to study. In particular, we then have yet another length scale given by the biexcitonc spatial extension. For these studies one should consider linear cross-polarized pulses.

# Zusammenfassung

Diese Dissertation behandelt zwei Themenkomplexe. Zunächst werden zwei unterschiedliche theoretische Methoden zur Berechnung der optischen linearen Polarisation verglichen. Die erste Methode basiert auf Bewegungsgleichungen der konfigurationsgemittelten optischen Polarisation. Hier entsteht neben der bekannten Vielteilchen-Hierarchie eine zweite Hierarchie von Gleichungen für unordnungsassistierte Polarisationen immer höheren Grades. Während die Vielteilchenhierarchie bei der Beschreibung kohärent getriebener Halbleiter exakt behandelt werden kann, ist dies für die unordnungsassistierten Polarisationen nicht möglich. Eine zweite Born'sche Näherung führt bekanntlich zu unphysikalischen Spektren. Erst eine zusätzliche Markov-Näherung bringt hier Abhilfe. Diese unbefriedigende Situation kann nur geklärt werden, wenn man eine zweite Methode auf das gleiche Modell anwendet, die frei von Näherungen ist. Dies ist das Tight-Binding Modell im Ortsraum mit nachfolgender Konfigurationsmittelung, das in der Vergangenheit vielfach mit Erfolg angewendet wurde. Allerdings stellt es unvergleichlich höhere Anforderungen an die Rechnerkapazität als die zuvor genannte Methode. Es zeigt sich, dass die Resultate beider Methoden zwar grob übereinstimmen, in Details aber Abweichungen existieren. Weiterhin wird daher mit dem Tight-Binding Modell gearbeitet.

Der zweite Themenkomplex befasst sich mit der Interpretation unordnungsinduzierter spektraler Eigenschaften von exzitonischen Resonanzen im sowohl linearen als auch nichtlinearen Regime. Im Detail wird die Verschiebung und Breite linearer exzitonischer Spektren als Funktion der Längenskala schwacher Unordnung studiert. Die Interpretation macht von dem schon seit längerem bekannten Mechanismus der durch die Relativbewegung verursachten Mittelung Gebrauch. Es zeigt sich, dass die Wirksamkeit dieser Mittelung entscheidend von der Längenskala der Unordnung abhängt, wobei der Bohr'sche Radius eine wichtige Rolle spielt. Für kleinere Längenskala hat man ein universelles Verhalten, nicht jedoch für größere.

Schließlich werden nichtlineare Spektren betrachtet, wie sie im Rahmen der Methode der "Two-Dimensional Fourier-Transform Spectroscopy" (2DFTS) erhalten werden. Da diese Methode eine Variante des Vierwellenmischens darstellt, ist sie in der Lage, Information über homogene und inhomogene Breite getrennt zu liefern, im Gegensatz zur linearen Antwort. Da die Unordnung die Impulserhaltung der Schwerpunktsbewegung des Exzitons verletzt, kommt es zu zusätzlichen Kopplungen. Gerade die 2DFTS-Methode zeigt Kopplungen in sehr klarer Weise, wenn man erst einmal gelernt hat, wie man die Spektren zu lesen hat. Um dies zu erreichen, wird in einer Serie von einfachen Niveau-Systemen zunehmender Komplexität das 2DFT

Spektrum jeweils berechnet und dargestellt, bis man schließlich die Fano-Situation erreicht hat. Es zeigt sich, dass die aus dem Halbleitermodell berechneten Spektren solche spektralen Merkmale aufweisen, wie sie für Fano-Systeme gefunden wurden. Die Auswertung dieser Spektren liefert dann für den ungeordneten Fall eine homogene Breite, die um ca. 20 % größer ist als die für den geordneten Fall. Dies zeigt den Effekt des "unordnungs-induzierten Dephasierens", der schon früher für ein nichtwechselwirkendes System mit großer Unordnung vorhergesagt wurde. Es zeigt sich auch, dass man die Spektren des ungeordneten Halbleiters als inhomogene Linie interpretieren kann, deren einzelne homogene Linien durch eine mit der Energie zunehmende Dephasierungsrate gekennzeichnet sind. Auch dieser Effekt basiert auf einem Fano-Mechanismus.

Die Erkenntnisse dieser Arbeit sollen in naher Zukunft auf experimentelle Resultate angewendet werden, die mit der Methodes der 2DFTS erhalten wurden.

# Appendix

## Appendix A

### Abbreviation

| | |
|---|---|
| com | center of mass |
| FWHM | full width at half maximum |
| FWM | four-wave mixing |
| HF | Hartree-Fock |
| hh | heavy hole |
| PB | Pauli blocking |
| 2DFTS | two-dimensional Fourier-transform spectroscopy |

# Appendix B

## Coulomb matrix element

The Coulomb matrix element $V_q$ in Eq. (13), which is used to calculate the linear absorption in the k-space approach, is given by the Fourier-transform of the Coulomb-interaction matrix element $V(z)$ which for our one-dimensional model is given by [25]

$$V(z) = \frac{V_0}{\sqrt{z^2 + \left(\frac{4R}{\pi}\right)^2}} \tag{73}$$

as

$$V_q = \frac{2}{\mathcal{L}} K_0 \left( |q| \frac{4R}{\pi} \right) \tag{74}$$

with the normalizing length $\mathcal{L}$ and regularization length R=8.25 nm. $K_0(x)$ is the modified Bessel function.

In the real space tight-binding model the Coulomb interaction matrix element $V_{ij}$ is accordingly given as

$$V_{ij} = \frac{V_0}{\sqrt{(i-j)^2 a^2 + \left(\frac{4R}{\pi}\right)^2}}. \tag{75}$$

The regularized Coulomb matrix element, which is used in the 2DFT calculations, is given by [41]

$$V_{ij} = \frac{V_0}{|i-j|a - a_0}, \tag{76}$$

$a$ is the site separation and $a_0 = 0.5a$ is the regularization length. $V_0$ is a positive constant, which is chosen such that the binding energy has a value close to a real semiconductor system.

# Appendix C

## Cluster expansion

Many-body correlations of order $N$ consist of $N$ fermionic creation operators and $N$ annihilation operators. To truncate the hierarchy problem, one has to find a consistent way of approximating $\langle O_N \rangle$, which describes an $N$-particle operator [24,27]:

$$\begin{aligned}
\langle O_2 \rangle &= \langle O_2 \rangle_S + \Delta\langle O_2 \rangle && (77)\\
\langle O_3 \rangle &= \langle O_3 \rangle_S + \langle O_1 \rangle \Delta\langle O_2 \rangle + \Delta\langle O_3 \rangle && (78)\\
&\vdots \\
\langle O_N \rangle &= \langle O_N \rangle_S + \langle O_{N-2} \rangle_S \Delta\langle O_2 \rangle + \langle O_{N-4} \rangle \Delta\langle O_2 \rangle \Delta\langle O_2 \rangle + \ldots + \Delta\langle O_N \rangle. && (79)
\end{aligned}$$

Each term denotes a sum over all possibilities to reorganize the $N$ coordinates among singlets, doublets, etc. The lowest-level truncation scheme resulting from the cluster expansion is the singlet approximation which is identical to the Hartree-Fock approximation. The Hartree-Fock approximation, in which the full density matrix is represented by singlets, represents only the first step of the general cluster expansion. The next step to improve the level of approximation is to include also doublets. In this case, the full density matrix can describe uncorrelated carriers and an arbitrary amount of correlated pairs. The quantities $\Delta\langle O_N \rangle$ contain only the purely correlated part of the $N$-particle cluster. The advantage of the factorization is its direct physical interpretation.

# Appendix D

## Markov approximation

Here we follow the work of Hoyer [25]. We consider a general equation,

$$i\hbar\frac{\partial}{\partial t}X(t) = \left(E_X - i\gamma\right) X(t) + A(t). \tag{80}$$

Its formal solution is given by

$$X(t) = -\frac{i}{\hbar}\int_{\infty}^{t} A_j(t')e^{-\frac{i}{\hbar}(E_X - i\gamma)(t-t')}dt'. \tag{81}$$

In order to separate the strongly and weakly time dependent terms under the integral, we assume that $A(t)$ itself is mainly oscillating with a frequency $E_A/\hbar$ and can be written as

$$A(t) = A_0(t)e^{-\frac{i}{\hbar}E_A t}, \tag{82}$$

where $A_0(t)$ is slowly varying in time. Then we can take the slowly varying part out of the integral and integrate, obtaining:

$$X(t) \approx \frac{A(t)}{E_A - E_X + i\gamma}. \tag{83}$$

More generally:

$$i\hbar\frac{\partial}{\partial t}X(t) = \left(E_X - i\gamma\right) X(t) + \sum_j A_j(t) \quad \Rightarrow \quad X(t) \approx \sum_j \frac{A_j(t)}{E_{A_j} - E_X + i\gamma}. \tag{84}$$

# Appendix E

## Equations

Here we present the derivation of various equations of motion in the linear response applying the rotating-wave approximation and the low-density limit.

### k-space equations

*With second-Born, without Markov approximation, correlated disorder:*

$$\begin{aligned} i\hbar\frac{\partial}{\partial t}\langle p_{kk}\rangle_E = {}& (\varepsilon_k^c - \varepsilon_k^v + \sum_{q\neq k} V_{k-q} - \frac{i\hbar}{T_2})\langle p_{kk}\rangle_E - E(t)d_{vc}^* - \sum_{q\neq k} V_{k-q}\langle p_{qq}\rangle_E \\ & + \sum_q (\langle U_{k-q}^c p_{kq}\rangle_E - \langle U_{q-k}^v p_{qk}\rangle_E) \end{aligned} \tag{85}$$

$$\begin{aligned} i\hbar\frac{\partial}{\partial t}\langle U_{k-l}^c p_{kl}\rangle_E = {}& (\varepsilon_l^c - \varepsilon_k^v + \sum_{q\neq k} V_{k-q} - \frac{i\hbar}{T_2})\langle U_{k-l}^c p_{kl}\rangle_E - \sum_{q\neq k} V_{k-q}\langle U_{k-l}^c p_{q,l-k+q}\rangle_E \\ & + \langle U_{k-l}^c U_{l-k}^c\rangle_E\langle p_{kk}\rangle_E - \langle \mathbf{U_{k-l}^c U_{l-k}^v}\rangle_\mathbf{E}\langle \mathbf{p_{ll}}\rangle_\mathbf{E} \end{aligned} \tag{86}$$

$$\begin{aligned} i\hbar\frac{\partial}{\partial t}\langle U_{k-l}^v p_{kl}\rangle_E = {}& (\varepsilon_l^c - \varepsilon_k^v + \sum_{q\neq k} V_{k-q} - \frac{i\hbar}{T_2})\langle U_{k-l}^v p_{kl}\rangle_E - \sum_{q\neq k} V_{k-q}\langle U_{k-l}^v p_{q,l-k+q}\rangle_E \\ & + \langle \mathbf{U_{k-l}^v U_{l-k}^c}\rangle_\mathbf{E}\langle \mathbf{p_{kk}}\rangle_\mathbf{E} - \langle U_{k-l}^v U_{l-k}^v\rangle_E\langle p_{ll}\rangle_E \end{aligned} \tag{87}$$

*With Markov approximation, correlated disorder:*

$$\begin{aligned} i\hbar\frac{\partial}{\partial t}\langle p_{kk}\rangle_E = {}& \left(\varepsilon_k^c - \varepsilon_k^v + \sum_{q\neq k} V_{k-q} - \frac{i\hbar}{T_2}\right)\langle p_{kk}\rangle_E - E(t)d_{vc}^* - \sum_{q\neq k} V_{k-q}\langle p_{qq}\rangle_E \\ & + \sum_{q,q'}\Bigg(\langle U_{k-q}^c U_{q-q'}^c\rangle_E \frac{\langle p_{kq'}\rangle_E}{\varepsilon_{q'}^c - \varepsilon_q^c + \frac{i\hbar}{T_2}} - \langle \mathbf{U_{k-q}^c U_{q'-k}^v}\rangle_\mathbf{E}\frac{\langle \mathbf{p_{q'q}}\rangle_\mathbf{E}}{\varepsilon_\mathbf{k}^\mathbf{v} - \varepsilon_\mathbf{q'}^\mathbf{v} + \frac{\mathbf{i\hbar}}{\mathbf{T_2}}} \\ & - \langle \mathbf{U_{q-k}^v U_{k-q'}^c}\rangle_\mathbf{E}\frac{\langle \mathbf{p_{qq'}}\rangle_\mathbf{E}}{\varepsilon_\mathbf{q'}^\mathbf{c} - \varepsilon_\mathbf{k}^\mathbf{c} + \frac{\mathbf{i\hbar}}{\mathbf{T_2}}} + \langle U_{q-k}^v U_{q'-q}^v\rangle_E \frac{\langle p_{q'k}\rangle_E}{\varepsilon_q^v - \varepsilon_{q'}^v + \frac{i\hbar}{T_2}}\Bigg) \end{aligned} \tag{88}$$

For anticorrelated disorder bold-faced terms have opposite signs. For uncorrelated disorder they vanish.

### exciton basis, all excitonic states

By transforming the equations into an exciton basis we obtain the following equations.

*With second-Born, without Markov approximation:*

$$\begin{aligned} i\hbar\frac{\partial}{\partial t}\langle X_{\nu 0}\rangle_E =& E_\nu\langle X_{\nu 0}\rangle_E - E(t)d^*_{vc}\sum_{\tilde{k}}\phi^*_\nu(\tilde{k}) \\ &+\sum_{\nu'}\sum_{q_1}\Bigg(\langle X_{\nu',-q_1}U^c_{q_1}\rangle_E\sum_{\tilde{k}}\phi^*_\nu(\tilde{k})\phi_{\nu'}(\tilde{k}-q^h_1) \\ &\qquad - \langle X_{\nu',-q_1}U^v_{q_1}\rangle_E\sum_{\tilde{k}}\phi^*_\nu(\tilde{k})\phi_{\nu'}(\tilde{k}+q^e_1)\Bigg) \end{aligned} \tag{89}$$

$$\begin{aligned} i\hbar\frac{\partial}{\partial t}\langle X_{\nu q}U^c_{-q}\rangle_E =& \left(E_\nu+\frac{\hbar^2q^2}{2M}\right)\langle X_{\nu q}U^c_{-q}\rangle_E \\ &+\sum_{\nu'}\sum_{q_1}\langle X_{\nu',q-q_1}\rangle_E\Bigg(\langle U^c_{-q}U^c_{q_1}\rangle_E\sum_{\tilde{k}}\phi^*_\nu(\tilde{k})\phi_{\nu'}(\tilde{k}-q^h_1) \\ &\qquad -\langle\mathbf{U^c_{-q}U^v_{q_1}}\rangle_{\mathbf{E}}\sum_{\tilde{\mathbf{k}}}\phi^*_\nu(\tilde{\mathbf{k}})\phi_{\nu'}(\tilde{\mathbf{k}}+\mathbf{q^e_1})\Bigg) \end{aligned} \tag{90}$$

$$\begin{aligned} i\hbar\frac{\partial}{\partial t}\langle X_{\nu q}U^v_{-q}\rangle_E =& \left(E_\nu+\frac{\hbar^2q^2}{2M}\right)\langle X_{\nu q}U^v_{-q}\rangle_E \\ &+\sum_{\nu'}\sum_{q_1}\langle X_{\nu',q-q_1}\rangle_E\Bigg(\langle\mathbf{U^v_{-q}U^c_{q_1}}\rangle_{\mathbf{E}}\sum_{\tilde{\mathbf{k}}}\phi^*_\nu(\tilde{\mathbf{k}})\phi_{\nu'}(\tilde{\mathbf{k}}-\mathbf{q^h_1}) \\ &\qquad - \langle U^v_{-q}U^v_{q_1}\rangle_E\sum_{\tilde{k}}\phi^*_\nu(\tilde{k})\phi_{\nu'}(\tilde{k}+q^e_1)\Bigg) \end{aligned} \tag{91}$$

*With Markov approximation:*

$$\begin{aligned} i\hbar\frac{\partial}{\partial t}\langle X_{\nu 0}\rangle_E =& E_\nu\langle X_{\nu 0}\rangle_E - E(t)d^*_{vc}\sum_{\tilde{k}}\phi^*_\nu(\tilde{k}) \\ &+\sum_{\nu'}\sum_{q_1}\sum_{\nu''}\sum_{q_2}\Bigg(\frac{\langle X_{\nu'',-q_1-q_2}\rangle_E}{E_{\nu''}-E_{\nu'}+\frac{\hbar^2q_2^2}{2M}+\frac{\hbar^2 2q_1q_2}{2M}+i\gamma}\cdot \\ &\Bigg[\langle U^c_{q_1}U^c_{q_2}\rangle_E\sum_{\tilde{k}}\phi^*_{\nu'}(\tilde{k})\phi_{\nu''}(\tilde{k}-q^h_2)\sum_{\tilde{k}}\phi^*_\nu(\tilde{k})\phi_{\nu'}(\tilde{k}-q^h_1) \\ &-\langle\mathbf{U^c_{q_1}U^v_{q_2}}\rangle_{\mathbf{E}}\sum_{\tilde{\mathbf{k}}}\phi^*_{\nu'}(\tilde{\mathbf{k}})\phi_{\nu''}(\tilde{\mathbf{k}}+\mathbf{q^e_2})\sum_{\tilde{\mathbf{k}}}\phi^*_\nu(\tilde{\mathbf{k}})\phi_{\nu'}(\tilde{\mathbf{k}}-\mathbf{q^h_1}) \\ &-\langle\mathbf{U^v_{q_1}U^c_{q_2}}\rangle_{\mathbf{E}}\sum_{\tilde{\mathbf{k}}}\phi^*_{\nu'}(\tilde{\mathbf{k}})\phi_{\nu''}(\tilde{\mathbf{k}}-\mathbf{q^h_2})\sum_{\tilde{\mathbf{k}}}\phi^*_\nu(\tilde{\mathbf{k}})\phi_{\nu'}(\tilde{\mathbf{k}}+\mathbf{q^e_1}) \\ &+\langle U^v_{q_1}U^v_{q_2}\rangle_E\sum_{\tilde{k}}\phi^*_{\nu'}(\tilde{k})\phi_{\nu''}(\tilde{k}+q^e_2)\sum_{\tilde{k}}\phi^*_\nu(\tilde{k})\phi_{\nu'}(\tilde{k}+q^e_1)\Bigg]\Bigg) \end{aligned} \tag{92}$$

If we introduce the notation:

$$U_{ex}(\nu, \nu', q_1) = U^c_{q_1} \sum_{\tilde{k}} \phi^*_\nu(\tilde{k}) \phi_{\nu'}(\tilde{k} - q^h_1) - U^v_{q_1} \sum_{\tilde{k}} \phi^*_\nu(\tilde{k}) \phi_{\nu'}(\tilde{k} + q^e_1), \tag{93}$$

we cannot choose the anticorrelated and uncorrelated cases.

*In second-Born approximation:*

$$i\hbar \frac{\partial}{\partial t} \langle X_{\nu 0} \rangle_E = E_\nu \langle X_{\nu 0} \rangle_E - E(t) d^*_{vc} \sum_{\tilde{k}} \phi^*_\nu(\tilde{k}) + \sum_{\nu'} \sum_{q_1} \langle X_{\nu', -q_1} U_{ex}(\nu, \nu', q_1) \rangle_E \tag{94}$$

$$\begin{aligned} i\hbar \frac{\partial}{\partial t} \langle X_{\nu', -q_1} U_{ex}(\nu, \nu', q_1) \rangle_E = &\left( E_{\nu'} + \frac{\hbar^2 q_1^2}{2M} \right) \langle X_{\nu', -q_1} U_{ex}(\nu, \nu', q_1) \rangle_E \\ &+ \sum_{\nu''} \sum_{q_2} \langle X_{\nu'', -q_1 - q_2} \rangle_E \langle U_{ex}(\nu, \nu', q_1) U_{ex}(\nu', \nu'', q_2) \rangle_E \end{aligned} \tag{95}$$

*In second-Born - Markov approximation:*

$$\begin{aligned} i\hbar \frac{\partial}{\partial t} \langle X_{\nu 0} \rangle_E = &E_\nu \langle X_{\nu 0} \rangle_E - E(t) d^*_{vc} \sum_{\tilde{k}} \phi^*_\nu(\tilde{k}) \\ &+ \sum_{\nu'} \sum_{q_1} \sum_{\nu''} \sum_{q_2} \frac{\langle X_{\nu'', -q_1 - q_2} \rangle_E \langle U_{ex}(\nu, \nu', q_1) U_{ex}(\nu', \nu'', q_2) \rangle_E}{E_{\nu''} - E_{\nu'} + \frac{\hbar^2 q_2^2}{2M} + \frac{\hbar^2 2 q_1 q_2}{2M} + i\gamma} \end{aligned} \tag{96}$$

**1s exciton equations**

*With second-Born, without Markov approximation:*

$$\begin{aligned} i\hbar \frac{\partial}{\partial t} \langle X_0 \rangle_E = &E_0 \langle X_0 \rangle_E - E(t) d^*_{vc} \sum_{\tilde{k}} \phi^*(\tilde{k}) \\ &+ \sum_{q_1} \left( \langle X_{-q_1} U^c_{q_1} \rangle_E \sum_{\tilde{k}} \phi^*(\tilde{k}) \phi_(\tilde{k} - q^h_1) - \langle X_{-q_1} U^v_{q_1} \rangle_E \sum_{\tilde{k}} \phi^*(\tilde{k}) \phi(\tilde{k} + q^e_1) \right) \end{aligned} \tag{97}$$

$$\begin{aligned} i\hbar \frac{\partial}{\partial t} \langle X_q U^c_{-q} \rangle_E = &\left( E_0 + \frac{\hbar^2 q^2}{2M} \right) \langle X_q U^c_{-q} \rangle_E \\ &+ \sum_{q_1} \langle X_{q - q_1} \rangle_E \Bigg( \langle U^c_{-q} U^c_{q_1} \rangle_E \sum_{\tilde{k}} \phi^*(\tilde{k}) \phi_(\tilde{k} - q^h_1) \\ &- \langle \mathbf{U^c_{-q} U^v_{q_1}} \rangle_{\mathbf{E}} \sum_{\tilde{\mathbf{k}}} \phi^*(\tilde{\mathbf{k}}) \phi(\tilde{\mathbf{k}} + \mathbf{q^e_1}) \Bigg) \end{aligned} \tag{98}$$

$$
\begin{aligned}
i\hbar\frac{\partial}{\partial t}\langle X_q U^v_{-q}\rangle_E =& \left(E_0 + \frac{\hbar^2 q^2}{2M}\right)\langle X_q U^v_{-q}\rangle_E \\
&+ \sum_{q_1}\langle X_{q-q_1}\rangle_E \Bigg(\langle \mathbf{U^v_{-q} U^c_{q_1}}\rangle_{\mathbf{E}} \sum_{\tilde{\mathbf{k}}} \phi^*(\tilde{\mathbf{k}})\phi_(\tilde{\mathbf{k}} - \mathbf{q_1^h}) \\
&\qquad - \langle U^v_{-q} U^v_{q_1}\rangle_E \sum_{\tilde{k}} \phi^*(\tilde{k})\phi_(\tilde{k} + q_1^e)\Bigg)
\end{aligned}
\tag{99}
$$

*With Markov approximation:*

$$
\begin{aligned}
i\hbar\frac{\partial}{\partial t}\langle X_0\rangle_E =& E_0\langle X_0\rangle_E - E(t)d^*_{vc}\sum_{\tilde{k}}\phi^*(\tilde{k}) \\
&+ \sum_{q_1}\sum_{q_2}\left(\frac{\langle X_{-q_1-q_2}\rangle_E}{\frac{\hbar^2 q_2^2}{2M} + \frac{\hbar^2 2q_1 q_2}{2M} + i\gamma}\cdot\right. \\
&\Bigg[\langle U^c_{q_1} U^c_{q_2}\rangle_E \sum_{\tilde{k}}\phi^*(\tilde{k})\phi(\tilde{k} - q_2^h)\sum_{\tilde{k}}\phi^*(\tilde{k})\phi(\tilde{k} - q_1^h) \\
&-\langle \mathbf{U^c_{q_1} U^v_{q_2}}\rangle_{\mathbf{E}} \sum_{\tilde{\mathbf{k}}}\phi^*(\tilde{\mathbf{k}})\phi(\tilde{\mathbf{k}} + \mathbf{q_2^e})\sum_{\tilde{\mathbf{k}}}\phi^*(\tilde{\mathbf{k}})\phi(\tilde{\mathbf{k}} - \mathbf{q_1^h}) \\
&-\langle \mathbf{U^v_{q_1} U^c_{q_2}}\rangle_{\mathbf{E}} \sum_{\tilde{\mathbf{k}}}\phi^*(\tilde{\mathbf{k}})\phi(\tilde{\mathbf{k}} - \mathbf{q_2^h})\sum_{\tilde{\mathbf{k}}}\phi^*(\tilde{\mathbf{k}})\phi(\tilde{\mathbf{k}} + \mathbf{q_1^e}) \\
&\left. + \langle U^v_{q_1} U^v_{q_2}\rangle_E \sum_{\tilde{k}}\phi^*(\tilde{k})\phi(\tilde{k} + q_2^e)\sum_{\tilde{k}}\phi^*(\tilde{k})\phi(\tilde{k} + q_1^e)\Bigg]\right)
\end{aligned}
\tag{100}
$$

With the notation:

$$
U_{ex}(q_1) = U^c_{q_1}\sum_k \phi^*(k)\phi(k - q_1^h) - U^v_{q_1}\sum_k \phi^*(k)\phi(k + q_1^e)
\tag{101}
$$

*Only second-Born approximation:*

$$
i\hbar\frac{\partial}{\partial t}\langle X_0\rangle_E = \left(E_0 - \frac{i\hbar}{T_2}\right)\langle X_0\rangle_E + \sum_{q_1}\langle X_{-q_1}U_{ex}(q_1)\rangle_E - E(t)d^*_{vc}\sum_{\tilde{k}}\phi^*(\tilde{k})
\tag{102}
$$

$$
i\hbar\frac{\partial}{\partial t}\langle X_{-q_1}U_{ex}(q_1)\rangle_E = \left(E_0 + \frac{\hbar^2 q_1^2}{2M} - \frac{i\hbar}{T_2}\right)\langle X_{-q_1}U_{ex}(q_1)\rangle_E
\tag{103}
$$

$$
+\sum_{q_2}\langle X_{-q_1-q_2}\rangle_E\langle U_{ex}(q_1)U_{ex}(q_2)\rangle_E
\tag{104}
$$

*With Markov approximation:*

$$
i\hbar\frac{\partial}{\partial t}\langle X_0\rangle_E = \left(E_0 - \frac{i\hbar}{T_2}\right)\langle X_0\rangle_E + \sum_{q_1}\sum_{q_2}\frac{\langle X_0\rangle_E\langle U_{ex}(q_1)U_{ex}(-q_2)\rangle_e}{\frac{\hbar^2 q_1^2}{2M} + \frac{\hbar^2 q_1 q_2}{2M} + \frac{i\hbar}{T_2}} - E(t)d^*_{vc}\sum_{\tilde{k}}\phi^*(\tilde{k})
\tag{105}
$$

If we use that $\langle U_{ex}(q_1)U_{ex}(q_2)\rangle_E \propto \delta_{q_1,-q_2}$:

*With second-Born approximation:*

$$i\hbar\frac{\partial}{\partial t}\langle X_0\rangle_E \;= \left(E_0 - \frac{i\hbar}{T_2}\right)\langle X_0\rangle_E + \sum_{q_1}\langle X_{-q_1}U_{ex}(q_1)\rangle_E - E(t)d^*_{vc}\sum_{\tilde{k}}\phi^*(\tilde{k}) \tag{106}$$

$$i\hbar\frac{\partial}{\partial t}\langle X_{-q_1}U_{ex}(q_1)\rangle_E = \left(E_0 + \frac{\hbar^2 q_1^2}{2M} - \frac{i\hbar}{T_2}\right)\langle X_{-q_1}U_{ex}(q_1)\rangle_E + \langle X_0\rangle_E\langle U_{ex}(q_1)U_{ex}(-q_1)\rangle_E \tag{107}$$

*Second-Born - Markov approximation:*

$$i\hbar\frac{\partial}{\partial t}\langle X_0\rangle_E \;= \left(E_0 - \frac{i\hbar}{T_2} + \sum_{q_1}\frac{\langle U_{ex}(q_1)U_{ex}(-q_1)\rangle_E}{-\frac{\hbar^2 q_1^2}{2M} + \frac{i\hbar}{T_2}}\right)\langle X_0\rangle_E - E(t)d^*_{vc}\sum_{\tilde{(}k)}\phi^*(\tilde{(}k)) \tag{108}$$

# Appendix F

## Mathematical explanation of the double-peaked spectrum with second Born approximation

Here we follow Zimmermann [29]. The appearance of the two-peak structure of the spectrum, which is certainly unphysical, can most easily be understood by considering the lowest-energy exciton.

$$i\hbar\frac{\partial}{\partial t}\langle X_0\rangle_E = (E_0 - i\gamma)\,\langle X_0\rangle_E + \sum_q \langle X_{-q}U_{ex}(q)\rangle_E - E(t)d^*_{vc}\sum_{\tilde{k}}\phi^*(\tilde{k}) \tag{109}$$

$$i\hbar\frac{\partial}{\partial t}\langle X_{-q}U_{ex}(q)\rangle_E = \left(E_0 + \frac{\hbar^2 q^2}{2M} - \frac{i\hbar}{T2}\right)\langle X_{-q}U_{ex}(q)\rangle_E + \langle X_0\rangle_E\langle U_{ex}(q)U_{ex}(-q)\rangle_E \tag{110}$$

The formal solution for the exciton amplitude can be obtained by Fourier transformation as

$$\hbar\omega\langle X_0(\omega)\rangle_E = (E_0 - i\gamma)\langle X_0(\omega)\rangle_E + \sum_q \langle U_{exc}(q)X_{-q}(\omega)\rangle_E - E(\omega)d^*_{vc}\sum_{\tilde{k}}\phi^*(\tilde{k}) \tag{111}$$

where the disorder-assisted amplitude follows from

$$\hbar\omega\langle U_{exc}(q)X_{-q}(\omega)\rangle_E = (E_0+\frac{\hbar^2 q^2}{2M}-i\gamma)\langle U_{exc}(q)X_{-q}(\omega)\rangle_E+\langle U_{exc}(q)U_{exc}(-q)\rangle_E\langle X_0(\omega)\rangle_E \tag{112}$$

thus

$$\langle U_{exc}(q)X_{-q}(\omega)\rangle_E = \frac{\langle U_{exc}(q)U_{exc}(-q)\rangle_E\langle X_0(\omega)\rangle_E}{\hbar\omega - E_0 - \frac{\hbar^2 q^2}{2M} + i\gamma}. \tag{113}$$

Finally

$$\left(\hbar\omega - E_0 - \frac{\hbar^2 q^2}{2M} + i\gamma + \sigma\right)\langle X_0(\omega)\rangle_E = E(\omega)d^*_{vc}\sum_{\tilde{k}}\phi^*(\tilde{k}), \tag{114}$$

where $\sigma$ is the self energy

$$\begin{aligned}\sigma = -\sum_q \frac{\langle U_{exc}(q)U_{exc}(-q)\rangle_E}{\hbar\omega - E_0 - \frac{\hbar^2 q^2}{2M} + i\gamma} &= -\sum_q PV\left(\frac{1}{\hbar\omega - E_0 - \frac{\hbar^2 q^2}{2M}}\right)\langle U_{exc}(q)U_{exc}(-q)\rangle_E \\ &\quad + i\pi\sum_q \delta\left(\hbar\omega - E_0 - \frac{\hbar^2 q^2}{2M}\right)\langle U_{exc}(q)U_{exc}(-q)\rangle_E\end{aligned} \tag{115}$$

where PV stands for principal value determining the real part $\sigma'$.

This expression for the self energy shows that it has an imaginary part $\sigma''$ only for photon energies $\hbar\omega$ that are above the lowest excitonic resonance at $E_0$ in the ordered system. Thus, for energies above $E_0$ we expect approximately a half-Lorentzian. For energies below $E_0$ a contribution to the spectrum solely arises from the zero of $\hbar\omega - E_q - \sigma'$, which leads to a broadened $\delta$-like peak there.

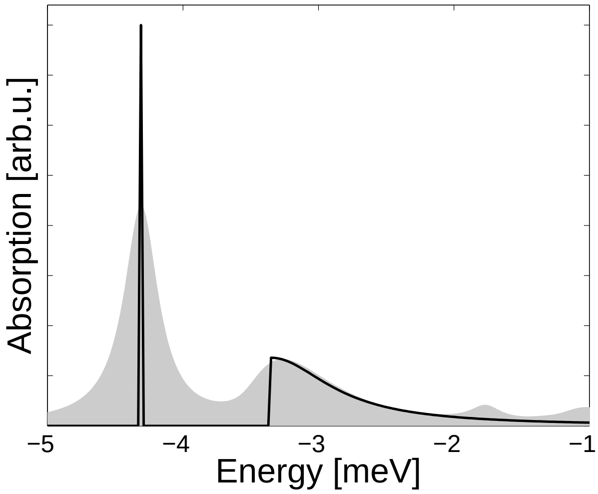

Figure 32: Calculated spectra in $k$-space with second-Born approximation (shaded area) and the theoretical result from the analytical solution

# Bibliography

[1] Ch.Lonsky, P.Thomas, and A.Weller: Optical Dephasing in Disordered Semiconductors, *Phys.Rev.Lett.*, **63**:652, 1989

[2] D.Brinkmann: Kohärente Dynamik wechselwirkender Teilchen in ungeordneten Halbleitern - Eine Modell-Studie, PhD Thesis, 1998, unpublished

[3] S.Weiser, T.Meier, J.Möbius, A.Euteneuer, E.J.Mayer, W.Stolz, M.Hofmann, W.W.Rühle, P.Thomas, and S.W.Koch: Disorder-induced dephasing in semiconductors, *Phys.Rev.B*, **61**:13088, 2000

[4] A.Thränhardt, S.Kuckenburg, A.Knorr, P.Thomas, and S.W.Koch: Interplay between coherent and incoherent scattering in quantum well secondary emission, *Phys.Rev.B*, **62**:16802, 2000

[5] A.Thränhardt: Exzitonendynamik und Sekundäremission in Halbleiterheterostrukturen, PhD Thesis, 2000, unpublished

[6] R.Zimmermann, E.Runge: Exciton lineshape in semiconductor quantum structures with interface roughness, *Journal of Luminescence*, **60 & 61**:320, 1994

[7] P.Bozsoki, P.Thomas, M.Kira, W.Hoyer, T.Meier, S.W.Koch, K.Maschke, I.Varga, and H.Stolz: Characterization of Disorder in Semiconductors via Single-Photon Interferometry, *Phys.Rev.Lett.*, **97**:227402, 2006

[8] F.Jahnke, M.Koch, T.Meier, J.Feldmann, W.Schäfer, P.Thomas, S.W.Koch, E.O.Göbel, and H. Nickel: Simultaneous influence of disorder and Coulomb interaction on photon echoes in semiconductors, *Phys.Rev.B*, **50**:8114, 1994

[9] J.Köhler, A.M.Jayannavar, and P.Reineker: Excitonic line shapes of disordered solids, *Z.Phys.B*, **75**:451, 1989

[10] H.Ludwig, E.Runge and R.Zimmermann: Exact calculation of distributions for excitonic oscillator strength and inverse participation ratio in disordered quantum wires, *Phys.Rev..B*, **67**:205302, 2003

[11] H.Overhof and K.Maschke: Exponential tails in optical absorption and electroabsorption of disordered systems - a one-dimensional model, *J.Phys. Condens.Matter*, **1**:431, 1989

[12] S.D.Baranovskii, U.Doerr, P.Thomas, A.Naumov, and W.Gebhardt: Exciton line broadening by compositional disorder in alloy quantum wells, *Phys.Rev.B*, **48**:17149, 1993

[13] S.D.Baranovskii and A.L.Efros: Band edge smearing in solid solutions, *Sov.Phys.Semicond*, **12**:1328, 1978

[14] R.Zimmermann, F.Große and E.Runge: Excitons in semiconductor nanostructures with disorder, *Pure & Appl. Chem.*, **69**:1179, 1997

[15] I.Kuznetsova, T.Meier, S.T.Cundiff, and P.Thomas: Determination of homogeneous and inhomogeneous broadening in semiconductor nanostructures by two-dimensional Fourier-transform optical spectroscopy, *Phys.Rev.B*, **76**:153301, 2007

[16] N.F.Schwabe and R.J.Elliott: Approximation of excitonic absorption in disordered systems using a compositional-component-weighted coherent-potential approximation, *Phys.Rev.B*, **53**:5318, 1996

[17] J. Singh (Editor): *Optical Properties of Condensed Matter and Applications*, Wiley, 2006

[18] T.Meier, P.Thomas, S.W.Koch: *Coherent Semiconductor Optics*, Springer, 2007

[19] X.Li, T.Zhang, C.N.Borca, and S.T.Cundiff: Many-Body Interactions in Semiconductors Probed by Optical Two-Dimensional Fourier Transform Spectroscopy, *Phys.Rev.Lett.*, **96**:057406, 2006

[20] I.Kuznetsova, P.Thomas, T.Meier, T.Zhang, X.Li, R.P.Mirin, and S.T.Cundiff: Signatures of many-particle correlations in two-dimensional Fourier-transform spectra of semiconductor nanostructures, *Sol.Stat.Comm.*, **142**:154, 2007

[21] T.Zhang, I.Kuznetsova, T.Meier, X.Li, R.P.Mirin, P.Thomas, and S.T.Cundiff: Polarization-dependent optical 2D Fourier transform spectroscopy of semiconductors, *PNAS*,**104**:14227, 2007

[22] D.S.Chelma and Jagdeep Shah: Many-body and correlation effects in semiconductors, *Nature*, **411**:549, 2001

[23] M. Kira, F. Jahnke, W.Hoyer, and S. W. Koch: Quantum theory of spontaneous emission and coherent effects in semiconductor microstructures, *Progress in Quantum Electronics*, **23**:189, 1999

[24] M. Kira, S. W. Koch: Many-body correlations and excitonic effects in semiconductor spectroscopy, *Progress in Quantum Electronics*, **30**:155, 2006

[25] W. Hoyer: Quantentheorie zu Exzitonbildung und Photolumineszenz in Halbleitern, PhD Thesis, 2002, unpublished

[26] K.Victor, V.M.Axt, and A.Stahl: Hierarchy of density matrices in coherent semiconductor optics, *Phys.Rev.B*, **51**:14164, 1995

[27] V.M.Axt, A.Stahl: A dynamics-controlled truncation scheme for the hierarchy of density matrices in semiconductor optics, *Z.Phys.B*, **93**:195, 1994

[28] K.Victor, V.M.Axt, G.Bartels, K.Bott, P.Thomas: Microscopic foundation of the phenomenological few-level approach to coherent semiconductor optics, *Z.Phys.B*, **99**:197, 1995

[29] R.Zimmermann: Private communication, based on: Exciton and disorder in semiconductor nanostructures, talk in Ráckeve in the frame of a Workshop of The International Research Training Group 790 "Electron-electron interactions in solids"

[30] H. Haug and S. W. Koch: *Quantum theory of the optical and electronic properties of semiconductors*, World Scientific Publ., Singapore, 3. edition, 1994

[31] P. Bozsoki: Microscopic modelling of photoluminescence in disordered semiconductors, PhD Thesis, 2005, unpublished

[32] F.Urbach: The Long-Wavelength Edge of Photographic Sensitivity and of the Electronic Absorption of Solids, *Phys.Rev.*, **92**:1324, 1953

[33] F.Moser and F.Urbach: Optical Absorption of Pure Silver Halides, *Phys.Rev.*, **102**:1519,1956

[34] M.V.Kurik: Urbach Rule, *phys.stat.sol. (a)*, **8**:9, 1971

[35] P. Bozsoki, S.D. Baranovskii, P. Thomas, and S.C. Agarwal: Potential fluctuations in disordered semiconductors measured by transport and optical methods, *phys. stat. sol. (c)*, **1**:113 (2004)

[36] S.T.Cundiff, T.Zhang: *Private communication*

[37] I.Kuznetsova: Investigation of semiconductor nanostructures by using optical two-dimensional Fourier-transform spectroscopy, PhD Thesis, 2007, unpublished

[38] T.Meier, A.Schulze, P.Thomas, H.Vaupel, and K.Maschke: Signatures of Fano resonances in four-wave-mixing experiments, *Phys.Rev.B*, **51**:13977, 1995

[39] I.Kuznetsova: *Private communication*

[40] T.F.Albrecht, K.Bott, T.Meier, A.Schulze, M.Koch, S.T.Cundiff, J.Feldmann, W.Stolz, P.Thomas, S.W.Koch, E.O.Göbel: Disorder mediated biexcitonic beats in semiconductor quantum wells, *Phys.Rev.B*, **54**:4436, 1996

[41] Ladislaus Bányai, Ian Galbraith, Claudia Ell, and Hartmut Haug: Excitons and biexcitons in semiconductor quantum wires, *Phys.Rev.B*, **36**:6099, 1987

## Acknowledgement

I would like to thank everyone who has contributed to the completion of this thesis in one way or another.

I am deeply indebted to my supervisor Prof. Peter Thomas for his support in helping me accomplish this work. His enduring patience and infinite understanding permitted to work in my own manner. His continuous encouragement helped me to swing over the low points during my work. Thank you for the anecdotes and the non-scientific activities which made the days colorful.

I thank Prof. Peter Thomas and Prof. Florian Gebhard for the opportunity to work and study in the European Graduate College "Electron-electron interactions in solids". In these years the different scientific activities (workshops, seminars) improved my skills which are required in the academic life.

I acknowledge the financial support by the European Graduate Collage and Prof. Stephan Koch.

I want to thank my colleagues for the pleasant working atmosphere and their useful advices. A special thank to Ada, Christina and Hanno for helping me whenever I had problems of any kind.

I would like to say thanks to some former colleagues, Peti, Irina and Walter for the many explanations, instructive discussions and efficient joint work even after they left our group.

I also thank Prof. Torsten Meier for his valuable comments and the opportunity to use the supercomputer facilities in Jülich.

I am glad to say thanks to "my Marburg family": Andi, Ági, Igor and Kornél. You always made sure that my life wasn't boring for a minute. I think my stay in Marburg wouldn't have been as eventful without all of you.

There is a big thanks towards my family (Mom, Dad, Norbi, Lili, Zsófi and Anett) for their constant support, and passionately believing in my capabilities. Thank you for accepting my decision to study in abroad. Although you live far away, you have been always there for me.

To everyone else that has been part of my wonderful Marburg-life and who I have failed to mention, thank you for the memories.

I wouldn't have done it without you.

Thank you. Danke. Köszönöm.

# Wissenschaftlicher Werdegang

NAME: Noémi Gőgh
GEBURTSDATUM: 16.05.1980
GEBURTSORT: Orosháza, Ungarn

| | |
|---|---|
| Jun 1998 | Abitur im Rózsa Ferenc Gymnasium, Békéscsaba, Ungarn |
| 1999-2004 | Studium der Physik an der József Attila Universität, Szeged, Ungarn |
| 18 Juni 2004 | Diplomabschluss im Fach Physik |
| 1 Juli 2005 | Begin des Promotionsstudiums an der Philipps-Universität Marburg |
| 2005-2009 | Mitglied des Graduiertenkollegs "Electron-electron interaction in solids" |
| 2008 | Wissenschaftliche Mitarbeiterin an der Philipps-Universität Marburg |